LJMU Research Online

Callanan, D, Longmore, SN, Battersby, C, Hatchfield, HP, Walker, DL, Henshaw, J, Keto, E, Barnes, A, Ginsburg, A, Kauffmann, J, Kruijssen, D, Lu, X, Mills, EAC, Pillai, T, Zhang, Q, Bally, J, Butterfield, N, Contreras, YA, Ho, LC, Immer, K, Johnston, KG, Ott, J, Patel, N and Tolls, V

 CMZoom III: Spectral Line Data Release

https://researchonline.ljmu.ac.uk/id/eprint/18644/

Article

CMZoom III: Spectral line data release

Daniel Callanan [1,2]★ Steven N. Longmore,[1] Cara Battersby,[2,3] H Perry Hatchfield,[3]
Daniel L. Walker [3,4] Jonathan Henshaw [1,5] Eric Keto,[2] Ashley Barnes [1,6,7] Adam Ginsburg,[8]
Jens Kauffmann,[9] J. M. Diederik Kruijssen [10] Xing Lu,[11] Elisabeth A. C. Mills,[12] Thushara Pillai,[13]
Qizhou Zhang,[2] John Bally,[14] Natalie Butterfield,[15] Yanett A. Contreras,[16] Luis C. Ho,[17,18]
Katharina Immer,[19] Katharine G. Johnston,[20] Juergen Ott,[21] Nimesh Patel[2] and Volker Tolls[2]

Affiliations are listed at the end of the paper

ABSTRACT

We present an overview and data release of the spectral line component of the SMA Large Program, *CMZoom*. *CMZoom* observed $^{12}CO\,(2–1)$, $^{13}CO\,(2–1)$, and $C^{18}O\,(2–1)$, three transitions of H_2CO, several transitions of CH_3OH, two transitions of OCS, and single transitions of SiO and SO within gas above a column density of $N(H_2) \geq 10^{23}\,cm^{-2}$ in the Central Molecular Zone (CMZ; inner few hundred pc of the Galaxy). We extract spectra from all compact 1.3 mm *CMZoom* continuum sources and fit line profiles to the spectra. We use the fit results from the $H_2CO\,3(0, 3)–2(0, 2)$ transition to determine the source kinematic properties. We find ∼90 per cent of the total mass of *CMZoom* sources have reliable kinematics. Only four compact continuum sources are formally self-gravitating. The remainder are consistent with being in hydrostatic equilibrium assuming that they are confined by the high external pressure in the CMZ. We find only two convincing proto-stellar outflows, ruling out a previously undetected population of very massive, actively accreting YSOs with strong outflows. Finally, despite having sufficient sensitivity and resolution to detect high-velocity compact clouds (HVCCs), which have been claimed as evidence for intermediate mass black holes interacting with molecular gas clouds, we find no such objects across the large survey area.

Key words: galaxies: nuclei – galaxies: star formation – submillimetre: galaxies.

1 INTRODUCTION

The central ∼500 pc of our Galaxy – the 'Central Molecular Zone' (CMZ) – provides a unique insight into the environmental dependence of the processes that govern star formation (Morris & Serabyn 1996; Longmore et al. 2013; Kruijssen et al. 2014; Henshaw et al. 2022). The conditions found within the CMZ – in particular the Mach number, densities, and temperatures of the gas, as well as the thermal and turbulent gas pressures – are far more extreme than those found in the Galactic disc, more closely resembling high-redshift galaxies (Kruijssen & Longmore 2013). The dense molecular gas in the CMZ, from which stars are expected to form, has been extensively studied both as part of large-scale Galactic plane surveys (e.g. Dame, Hartmann & Thaddeus 2001; Jackson et al. 2013; Longmore et al. 2017), as well as more targeted observations (e.g. Rodríguez-Fernández et al. 2004; Oka et al. 2007; Bally et al. 2010; Molinari et al. 2011; Jones et al. 2012; Mills & Morris 2013; Lu et al. 2015; Rathborne et al. 2015; Krieger et al. 2017; Lu et al. 2017; Mills & Battersby 2017; Kauffmann et al. 2017a, b; Ginsburg et al. 2018; Mills et al. 2018; Pound & Yusef-Zadeh 2018; Walker et al. 2018; Lu et al. 2019).

The *CMZoom* survey (Battersby et al. 2020) has aimed to fill a key unexplored part of observational parameter space by providing the first sub-pc spatial resolution survey of the CMZ at submillimetre wavelengths, targeting all dense gas above a column density of $N(H_2) \geq 10^{23}\,cm^{-2}$. The survey goals are to provide (i) a complete census of the most massive and dense cloud sources; (ii) the location, strength, and nature of strong shocks; (iii) the relationship of star formation to environmental conditions such as density, shocks, and large-scale flows.

A detailed overview of the *CMZoom* survey and the continuum data release was provided by Battersby et al. (2020, hereafter called 'Paper I'). Paper I found that while the CMZ has a larger average column density than the Galactic disc, the compact dense gas fraction (CDGF) is significantly lower. This is a measure of the fraction of a cloud that is contained within the compact substructures (i.e. overdensities) that may form or are currently forming stars. Paper I concludes that identifying and understanding the processes that inhibit the formation of compact substructures is vital in explaining the current dearth of star formation within the CMZ (Longmore et al. 2013; Kruijssen et al. 2014; Barnes et al. 2017; Henshaw et al. 2022).

The complete catalogue of compact (<10 arcsec) continuum sources was derived using dendrogram analysis and was presented in Hatchfield et al. (2020, hereafter called 'Paper II'). Two versions of this catalogue were produced: a robust catalogue that contains only sources detected with high confidence – i.e only sources with a peak flux and a mean flux that are 6σ and 2σ above the local RMS estimates of each mosaic, respectively – which was found to be 95 per cent complete at masses of $80\,M_\odot$ at a temperature of

Table 1. Summary of 10 key transitions targeted by the CMZoom survey with the percentage of sources investigated in this paper that show emission in that transition.

Molecule	Rest frequency (GHz)	Quantum number	Upper energy level (K)	Tracer	Detection percentage
^{12}CO	230.53800000	$J = 2$–1	16.59608	Dense gas	96
^{13}CO	220.39868420	$J = 2$–1	15.86618	Dense gas	96
$C^{18}O$	219.56035410	$J = 2$–1	15.8058	Dense gas	58
H_2CO	218.22219200	$3(0, 3)$–$2(0, 2)$	20.9564	Dense gas	82
H_2CO	218.47563200	$3(2, 2)$–$2(2, 1)$	68.0937	Dense gas	36
H_2CO	218.76006600	$3(2, 1)$–$2(2, 0)$	68.11081	Dense gas	39
SiO	217.10498000	5–4	31.25889	Protostellar outflows & shocks	39
OCS	218.90335550	18–17	99.81016	Shocks	15
OCS	231.06099340	19–18	110.89923	Shocks	13
SO	219.94944200	6–5	34.9847	Shocks	60

20 K, and a second catalogue focusing on completeness across the CMZ. This second 'high-completeness' catalogue was 95 per cent complete at masses of $50\,M_\odot$ at 20 K. The catalogues contain 285 and 816 sources, respectively. These sources have typical sizes of 0.04–0.4 pc, and are potential sites for ongoing and future star formation. Using this catalogue, Paper II estimates a maximum star forming potential in the CMZ of 0.08–$2.2\,M_\odot\,yr^{-1}$, though this drops to 0.04–$0.47\,M_\odot\,yr^{-1}$ when Sagittarius B2 – the dominant site of active star formation in the CMZ – is excluded.

In addition to the 230 GHz continuum data, the *CMZoom* survey also observed spectral line emission with an 8 GHz bandwidth using the ASIC correlator, and an additional 16 GHz using the SWARM correlator during later stages of the survey. In this paper, we give an overview of the spectral line data of the *CMZoom* survey, and present the full spectral data cubes where available, and cubes targeting specific transitions otherwise. The spectral set-up (detailed in Paper I) targeted a number of dense gas tracers (CO isotopologues, multiple H_2CO transitions) as well as key shock tracers (SiO, SO, OCS) and compact hot core tracers (CH_3OH, CH_3CN). An overview of the targeted lines is given in Table 1.

This paper is organized as follows. Section 2 details the additional steps required for the imaging pipeline for the spectral line data beyond that described for the continuum data in Paper I. Section 3 outlines the generation and fitting of spectra and the production of moment maps. Section 4 describes the data across the whole survey region, and then describes the data quality and summarizes the line detections on a per region basis. Section 5 uses the integrated intensity maps of all detected spectral lines to explore the relative variation in line emission across the survey as a rough indicator of variations in conditions throughout the CMZ. Section 6 examines the line properties of the *CMZoom* continuum sources identified in Paper II. By comparing the brightness, line fitting results, and detection statistics of different transitions, we aim to identify a primary kinematic tracer to describe the gas motions in the compact continuum sources. In Section 7, we use the results of the line fitting and conclusions in Section 6 to determine the likely virial state of the continuum sources, and search for signs of proto-stellar outflows and intermediate-mass black holes in the CMZoom line data.

2 OBSERVATIONS AND IMAGING

Here we summarize the source selection, spectral set-up, configurations, observing strategy, and data calibration, all of which discussed in more detail in Paper I and Paper II. In this section, we detail the

pipeline beyond these aspects, how this pipeline differs from that of continuum imaging, and the complexities and non-uniformities that arose during this process.

2.1 Observations and spectral set-up

Given the *CMZoom* survey's key goal of surveying the high-mass star formation across the entire CMZ, targets were selected to nearly completely include all regions of high-column density ($N(H_2) > 10^{23}\,cm^{-2}$), with one small exception detailed in Paper I. Additionally, several regions of interest with lower column density were selected, including the 'far-side candidate' clouds and isolated high-mass star forming region candidate clouds. A complete summary of source selection can be found in Section 2.1 of Paper I, and a region file with the mosaic of the survey's pointings is published in the Dataverse at https://dataverse.harvard.edu/dataverse/cmzoom.

Over the course of the program's observation, the SMA transitioned from the ASIC correlator to the SWARM correlator (Primiani et al. 2016), and the extent of each sideband in any given observation varies depending on the date of the observation. The early ASIC observations had a lower sideband covering 216.9–220.9 GHz and an upper sideband spanning 228.9–232.9 GHz, while the widest coverage in later SWARM observations spans 211.5–219.5 GHz in the lower sideband and 227.5–235.5 GHz in the upper sideband, with the majority of observations being intermediate to these two extremes. The spectral resolution is held consistent across all published observations at about 0.812 MHz (or about $1.1\,km\,s^{-1}$).

2.2 Imaging pipeline

Given the size of the survey both spatially and spectrally, a pipeline was developed to take the data from post-calibration to final imaging steps. We used the software package CASA[1] to ensure a consistent approach to data imaging across the whole survey, using both compact and subcompact SMA antenna configurations. In this section, we describe the stages of this pipeline.

The input for the pipeline is the source name (variable 'source-name') and the file paths corresponding to the relevant calibrated data sets in MIR[2] format. Each of these data sets are called into MIR, which we use to determine the associated correlator (or combination of correlators for observations taken within the middle of the

---

[1] https://casa.nrao.edu/
[2] https://lweb.cfa.harvard.edu/~cqi/mircook.html

observing period). Once this is determined, we use IDL2MIRIAD to convert the data from MIR to MIRIAD format. We split the data set into chunks, with the number of chunks depending on the correlator, before we flag the data. We enforced an eight channel and 100 channel flag for each chunk of data from the ASIC and SWARM correlators, respectively, to remove noisy channels from both edges of the bandpass. We then convert these flagged data into *uvfits* format using MIRIAD's *fits* command with *line* set to *channel*.

These *uvfits* files are then loaded into CASA and converted into a readable format using the *importuvfits* task in frequency mode with an LSRK outframe. They are then concatenated into full upper and lower sidebands for each correlator using *concat*. These sidebands are then continuum subtracted individually, using *uvcontsub*. We do this by estimating the baseline for all channels, excluding those surrounding the brightest line within each sideband, which in this case we took to be the ^{12}CO and ^{13}CO transitions for the upper and lower sidebands, respectively.

To image these continuum-subtracted data sets, we first generate a 'dirty' image cube to determine the appropriate R.M.S. noise level for the cleaning process. To do this, we run CASA's *tclean* task with 0 iterations over a patch of size 100×100 pixels around the phase center. We also perform this over a 100 channel subchunk of the whole frequency space to minimize the time taken. This channel range has been predetermined to be line-free by eye in all cubes. We then use *imstat* to calculate the average R.M.S. noise level throughout this cube.

Given the large variety of mosaic sizes and limited computing power, we implemented two separate methods to produce cleaned images. These methods are separated by image size, with a cut at 1000 pixels per spatial axis. For images smaller than this, we simply pass the full 4 GHz cube into a *tclean* task. We set the pixel size to 0.5 arcsec, corresponding to 6–8 pixels per roughly 3–4 arcsec beam. We used a *multiscale* deconvolver with scales equal to 0, 3, 9, and 27 arcsec to recover both large and small-scale structures. A channel width of 0.8 MHz, or 1.1 km s^{-1} was enforced to ensure consistency between ASIC and SWARM data sets. The weighting for each image was set to *briggs*, with a *robust* parameter of 0.5. The *threshold* is set to 5σ where possible, with σ calculated from the dirty cube previously discussed, with an arbitrarily high number (10^8) of *iterations* to ensure we reach this threshold. For some clouds, this 5σ threshold led to severe imaging artifacts so the threshold for these clouds were manually modified to remove them. We make use of the *chanchunks* parameter for these cleans, setting it to -1 to allow for the number of chunks that the data cube is split up into to be determined based on the available memory. We do not utilize the *automultithresh* parameter as used for the continuum images at this stage due to the significant increase in computational time of the pipeline that it leads to.

For images larger than the 1000 pixel cut described above, we instead clean separate subcubes surrounding a number of key spectral lines that the CMZoom survey targeted (see Table 1 for details). For the upper sideband, this is ^{12}CO(2–1) and OCS, and for the lower sideband we include three transitions of H$_2$CO in the range of 218–219 GHz, ^{13}CO(2–1), C^{18}O(2–1), SiO, OCS, and SO. Each of these cubes is 0.3 GHz wide, centred on the rest frequency of the corresponding transition, which is passed into the task within the *restfreq* parameter to allow for easy estimation of the velocity. All other parameters in these *tclean* tasks are the same as the smaller cubes.

Each output image is then primary beam corrected by dividing the image by the corresponding.pb file, which is generated by *tclean*, using CASA's *immath* task.

2.3 Catalog of continuum sources

The spectral fitting and subsequent analysis in this work makes use of the high-robustness version of the *CMZoom* catalogue, described in detail in Paper II. In this section, we provide a brief description of the source identification procedure and completeness properties.

The *CMZoom* catalogues are constructed using a pruned dendrogram. The dendrogram algorithm ASTRODENDRO is used to generate a hierarchical segmentation of the 1.3 mm dust continuum maps. Within this tree-like hierarchical representation, the highest level structures are defined as 'leaves', which correspond to compact dust continuum sources catalogued in Paper II. The catalogued leaves are uniquely determined by the choice of three initial dendrogram parameters: the dendrogram minimum value, the minimum significance parameter, and the minimum number of pixels to define a unique structure. The minimum significance and minimum value are both defined in reference to a global noise estimate, and the minimum number of pixels is selected relative to the typical beam of the SMA continuum observations. Because of the high variability in noise properties across 1.3 mm continuum within the CMZoom field, this initial dendrogram is overpopulated, particularly in regions with extreme local noise levels. A local estimate of the RMS noise is determined from the 1.3 mm continuum residuals, and is used to prune the dendrogram, removing sources with low local signal-to-noise ratios. The sources that remain in the high-robustness catalogue are dendrogram leaves that satisfy 6σ peak flux and 2σ mean flux minimum criteria relative to the local noise. The completeness of the catalogue is determined using simulated observations of the SMA's interferometric set-up, resulting in 95 per cent completeness to compact sources with masses above $80\,M_{\odot}$, assuming a dust temperature of 20 K. The final robust catalogue contains 285 compact sources, with effective radii between 0.04 and 0.4 pc, making them the potential progenitors of star clusters. In this work, we report on the spectral line properties of these 285 compact sources in the robust catalogue. A full description of the cataloging procedure is presented in Paper II.

# 3 SPECTRAL LINE FITTING AND MOMENT MAP GENERATION

In this section, we first describe the process used to identify and fit spectral line emission from the compact continuum sources identified in Paper II. We then describe the process used to create moment maps to show the spatial variation in line emission across the region.

Spectra for each compact continuum source identified in Paper II were produced by averaging all emission per channel over the mask produced for that leaf within the robust dendrogram catalogue in Paper II. These spectra were then fit using SCOUSEPY's[3] (Henshaw et al. 2016a, 2019) stand-alone fitter functionality (see also Barnes et al. 2021). We use a fiducial signal-to-noise ratio (SNR) of 5 to determine the initial threshold at which fits are accepted. The default kernel was set to 5, which smooths the spectrum by averaging every five channels. By-eye inspection showed that this produced reliable results for the majority of spectra. Approximately ∼5 per cent of spectra required manual fitting as the interactive SCOUSEPY fitter was unable to find a combination of SNR threshold and smoothing kernel to fit these spectra.

Before analysing these fits, we enforced a series of cuts to the data that by-eye inspection showed reliably removed bad fits. We

---

[3] https://github.com/jdhenshaw/scousepy
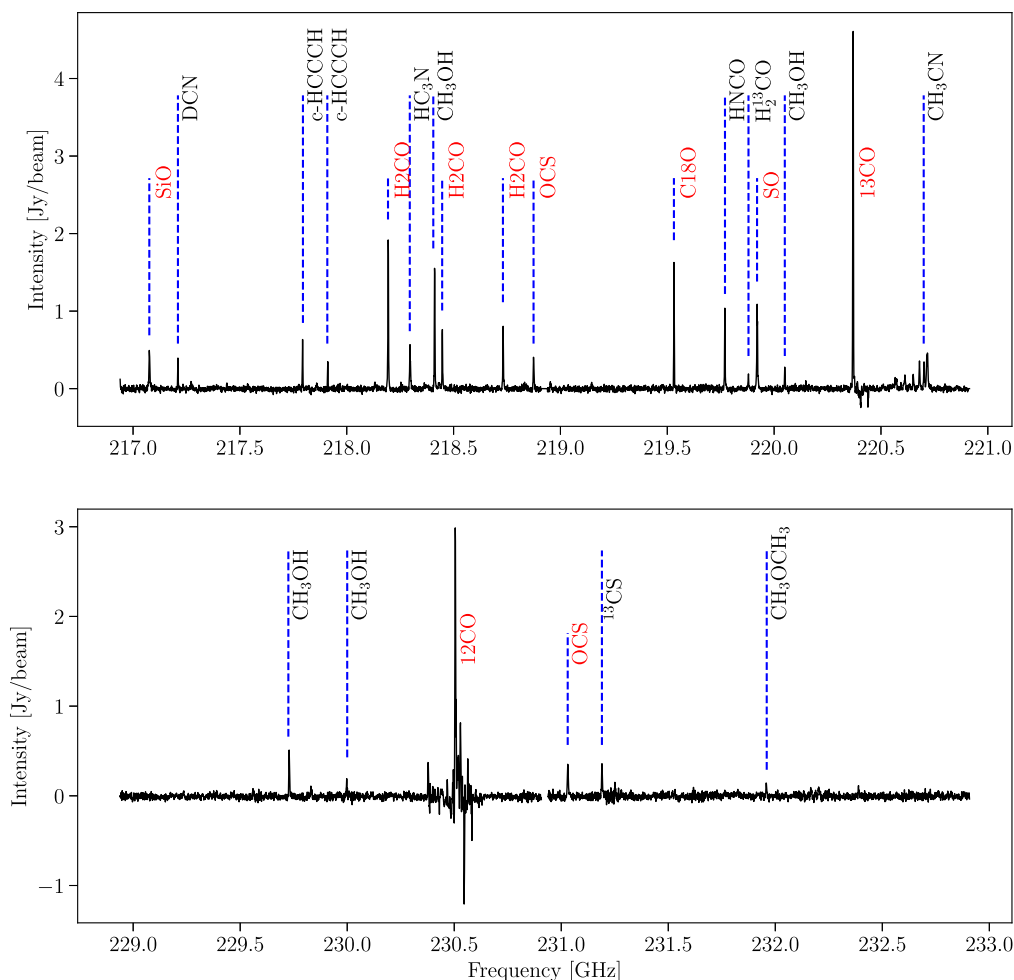
Figure 1. Complete spectra for the lower (top) and upper (bottom) sidebands for the region G0.380+0.050, colloquially referred to as 'cloud C'. Red labels indicates the 10 transitions targeted by the CMZoom survey, with over a dozen additional lines labeled in black. Assuming a beam size of 3×3 arcsec, at a frequency of 230 GHz, 1 Jy beam^{-1} = 2.57 K.

enforced a cut on the velocity dispersion, σ, and centroid velocity, V_{LSR}, uncertainties to only keep fits with uncertainties smaller than 1.5 km s^{-1}, and only allowed for a maximum uncertainty on the amplitude of 0.5 Jy beam^{-1} (1.3 K). To mitigate any issues with fitting multiple peaks as one single peak, we also cut-out any fits that had velocity dispersions larger than 20 km s^{-1}, and removed peaks narrower than 0.5 km s^{-1}. Despite this check, a manual assessment confirmed no spectral components that exceeded this upper velocity dispersion threshold. Due to a combination of imaging artefacts caused by spatial filtering, and inherently more complex spectra, the ^{12}CO and ^{13}CO spectral line fits were both deemed too unreliable throughout most of the survey and so were removed from this process.

The spectra show emission from a number of lines beyond the 10 key lines targeted by the survey (see Table 1). Fig. 1 shows the potential chemical complexity within a compact source in the CMZoom catalogue, using G0.380+0.040, or 'dust ridge cloud c', as an example. To identify these lines, a single V_{LSR} was determined for every compact source using the weighted average V_{LSR} of all detected lines. Any lines with a centroid velocity that differed by this V_{LSR} by more than ± 20 km s^{-1} were flagged as unidentified. These lines had their frequency calculated and then passed through

Splatalogue[4] with a search range of ± 0.04 GHz with an upper energy limit of 100 K. While this potentially misses some of the more high-excitation lines that may be present in the CMZ, this limit is simply a starting point to manually identify a first guess for each transition based on an assessment of the Einstein coefficient and upper energy level.

Once additional lines were assigned a most likely transition, we explored the quality of all the data by assessing the line of sight velocities, velocity dispersions, peak intensities, and root-mean-square (RMS) of each compact source in the survey.

Moment maps were then produced over a velocity range of ± 20 km s^{-1} surrounding all dendrogram sources within a region. To generate these moment maps, an RMS map was first produced by measuring the RMS per pixel and then cutting anything over a threshold as determined by the number of channels in each pixel. This robust RMS map was used to enforce a 10σ cut in order to identify the most significant emission within a region. This mask was then grown outwards, with SCIPY's *binary dilation* task, with a lower SNR cut, down to 5σ in order to detect low level extended

[4]https://splatalogue.online/

emission surrounding the most robust emission. Not all clouds have emission at the 10σ level, so this process was repeated with an iteratively lower SNR threshold until some emission was detected. If no emission was detected down to 5σ, the region was flagged as having no emission. Examples of these moment maps can be found in Appendix D, which has been made available online.

4 DATA PRESENTATION

Below we present the spectral line data cubes of the 10 main molecular line transitions covered in the CMZoom spectral set-up. Table 1 lists these transitions and their relevant properties.

We start by providing a summary of the general emission and absorption characteristics for each transition across the full survey region, focusing on comparing the spatial extent and velocity range of the emission for the different transitions and also with the 230 GHz continuum emission reported in Papers I and II. Our goal here is to provide the reader with a qualitative idea of the quality and the breadth of the data across the whole survey and on a per region basis.

Table 2 provides a description of the data quality for each of the 10 key transitions per region, and also highlights any issues which may affect the robustness and reliability of the images for analysis. We find that the ^{12}CO and ^{13}CO emission is detected in 100 and 90 per cent of the clouds, respectively. In nearly all clouds, the emission is spatially extended across a large fraction of the survey area. There is little correspondence between the ^{12}CO and ^{13}CO integrated intensity emission and the 230 GHz continuum emission. However, the ^{12}CO and ^{13}CO emission often suffers from severe imaging artefacts due to missing flux problems and also absorption from foreground gas clouds along the line of sight. For that reason, we urge caution in interpreting the integrated intensity and moment maps from these transitions, and more generally in blindly using the ^{12}CO and ^{13}CO data without the addition of zero-spacing information. Similarly, we have opted to not use these data products during the analysis until these imaging artefacts are resolved in a future paper unless there are particular aspects of the data which are relevant to highlight.

C^{18}O is detected towards 60 per cent of the clouds. The imaging artefacts are much less severe for C^{18}O than for the other CO transitions. The emission generally does appear spatially associated with the 230 GHz continuum emission.

SO and SiO are detected towards seven (20 per cent) and five (15 per cent) clouds, respectively, and are mostly well correlated – all clouds with detection SiO emission are also detected in SO. This is perhaps unsurprising given they are both species thought to trace shocks. We explore the correlation between different tracers more fully in Section 6.

As expected, the three H_2CO transitions show a very good correspondence, both spatially and in velocity. At least one transition of H_2CO was observed towards 50 per cent of clouds. In the spectra containing the H_2CO 3(2, 2)–3(2, 1) transition, there is often an apparent 'additional' velocity component offset by 50 km s^{-1} from the main velocity component that actually corresponds to CH$_3$OH-e (4(2)–3(1)) with a rest frequency of 218.4401 GHz.

A discussion of each of the CMZoom clouds in turn can be found in Appendix C, focusing on notable characteristics of the emission and specific issues with the data. The emission characteristics and issues for all clouds are summarized in Table 2. Through visual inspection of the spectral line data cubes and integrated intensity maps, we found that except where specifically mentioned, there is significant emission in all ^{12}CO and ^{13}CO cubes, often with strong emission and absorption over a V_{LSR} range of ± 100 km s^{-1}. However,

there are severe imaging artefacts, including strong negative bowls due to missing extended structure, making these cubes unreliable.

5 SPATIAL VARIATION IN LINE EMISSION ACROSS THE CMZ

With a fairly uniform sensitivity across the CMZ and a homogeneous analysis of the emission, CMZoom is well suited to investigating changes in line brightness on sub-pc scales as a function of location (Battersby et al. 2020). Detailed modelling of this line emission is required to fully understand the excitation conditions, opacity and chemistry to derive accurate physical properties of the gas. Such detailed modelling is beyond the scope of this paper. Instead in this section, we search for large differences in line strength ratios between clouds as a rough indicator of variations in conditions as a function of position throughout the CMZ.

For every region, if a transition was detected, all unmasked pixels in the moment map (see Section 3) were summed and compared to the total integrated intensity of C^{18}O and the 230 GHz continuum emission. Figs 2 and 3 show the distribution of these ratios as a function of Galactic longitude. Note that the Sgr B2 region (between $0.50° < l < 0.72°$), and the circumnuclear disc are not included on these figures due to the imaging difficulties described in Section C.

Comparing the longitude range of the different transitions, ^{12}CO and ^{13}CO are detected across the full survey extent. With the exception of G1.085–0.027, which has a strong OCS (231.1 GHz) detection, the ratios for all other transitions are confined to $|l| < 0.5°$.

As expected for a first look for general trends which does not solve for excitation, opacity, chemistry, etc., there is a large (order of magnitude) scatter in the line brightness ratios between clouds. Nevertheless, there are several interesting aspects of these figures, which we discuss below.

First, we find that ^{12}CO and ^{13}CO have the highest ratios and are detected within the most clouds, followed by C^{18}O, and then the lowest energy transition of H_2CO. This simple trend is, of course, expected given that these lines are the brightest and most extended across the cloud sample.
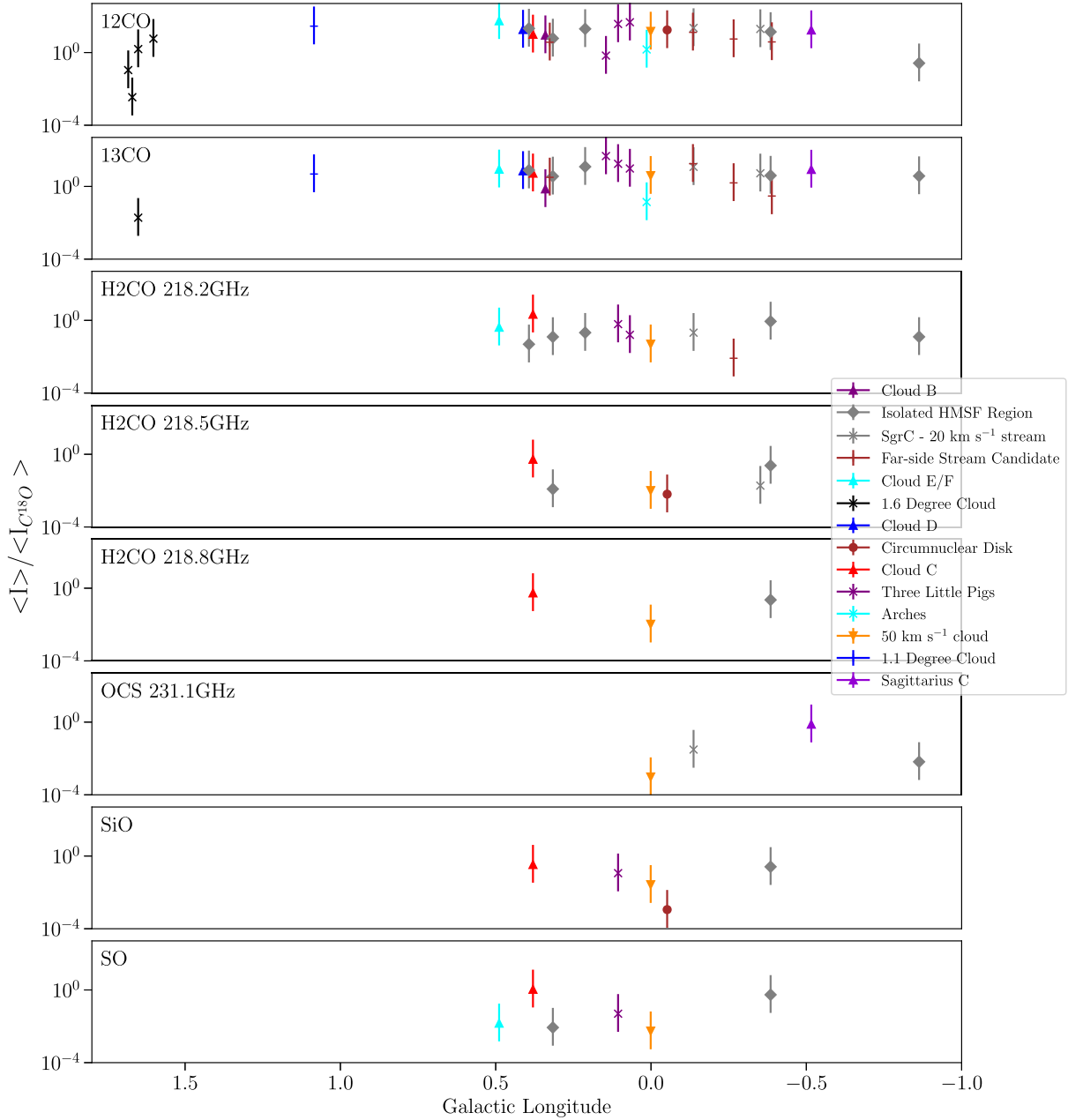
Secondly, the integrated intensity ratios with respect to dust emission of SO, SiO, and the two upper energy levels of H_2CO all increase by several orders of magnitude towards the Galactic Centre (i.e. as $|l| \to 0°$). Detailed modelling is required to understand the origin of this, but it is interesting to note that the highest excitation lines and shock tracers all increase in the same way, as may be expected due to changing physical conditions (e.g. increased shocks in the gas). This substantiates previous observations from Mills & Battersby (2017) who found a similar trend towards the Galactic Centre in a number of molecular species, a trend that was further supported by HC$_3$N observations by Mills et al. (2018) who found an increase in the dense gas fraction inwards of $R \lesssim 140$ pc.

Finally, we can compare the integrated intensity ratios of the CMZoom sources (all points apart from the grey diamonds in Figs 2 and 3) in the Galactic Centre with the isolated high-mass star-forming (HMSF) regions in the survey. These lie along our line of sight towards the CMZ but are actually located in the disc, providing a useful control sample.

The scatter of line brightness ratios of the isolated HMSF regions are consistent from the Galactic Centre sources in Figs 2 and 3. This is in direct contrast to observations of clouds in the Galactic Centre and the Galactic disc on $\gtrsim$ pc scales, which show very different emission integrated intensity ratios. Molecular line observations of clouds in

Table 2. Summary of conditions of data cubes for all clouds and across nine key molecular lines as a check of robustness and reliability for science. Each cube has been checked for a number of flags depending on extracted spectra and a visual inspection of the cubes. The flags are given as acronyms: multiple velocity components (MVC), imaging artefacts (IA), missing channels (MC), broad lines (GC), or narrow lines (N), line-wings (LW), non-detection (ND), and contamination of other spectral lines (C).

Sourcename	Colloquial name	^{13}CO	$C^{18}O$ (218.2 GHz)	H_2CO (218.5 GHz)	H_2CO (218.8 GHz)	H_2CO (218.9 GHz)	OCS (231.1 GHz)	OCS	SiO	SO
G0.001-0.058	50 km s^{-1} Cloud	IA	MVC	MVC	MVC	–	MC	ND	MVC	MVC
G0.014+0.021	Arches e1	–	ND	ND	MC	MC	MC	MC	ND	ND
G0.0.68+0.075	Three Little Pigs: Stone Cloud	IA	MVC	GC, MVC	MVC, C	MVC, GC	MC	ND	ND	ND
G0.070-0.035	Apex H$_2$CO bridge									
G0.106-0.082	Three Little Pigs: Sticks Cloud	IA	MVC	MVC, C	MVC	MC	ND	GC, LW	LW	–
G0.145-0.086	Three Little Pigs: Straw Cloud	IA	MVC	MVC	ND	MC	MC	–	ND	ND
G0.212-0.001	isolated HMSF candidate	IA	–	–	MVC	–	MC	MC	MC	ND
G0.316-0.201	isolated HMSF candidate	–	–	C	C	–	MC	MC	–	ND
G0.326-0.085	far-side stream candidate	IA	ND	ND	ND	ND	MC	MC	ND	ND
G0.340+0.055	Dust Ridge: Cloud b	IA	ND	–	ND	ND	MC	MC	ND	ND
G0.380+0.050	Dust Ridge: Cloud c	MVC	C	C	C	C	MC	MVC, MC	C	MVC, C
G0.393-0.034	isolated HMSF candidate	–	MVC	MVC	ND	ND	MC	MC	ND	ND
G0.412+0.052	Dust Ridge: Cloud d	IA	–	–	–	ND	MC	MC, ND	ND	ND
G0.489+0.010	Dust Ridge: Clouds e+f	–	–	–	–	–	MC, ND	–	–	–
G1.085-0.027	1.1° cloud	–	–	ND	ND	MC	MC	–	ND	ND
G1.602+0.018	1.6° cloud	MVC	ND	C	C	MC, ND	MC	ND	–	–
G1.651-0.050	1.6° cloud	ND	–	–	C	MC	MC	MC	ND	ND
G1.670-0.130	1.6° cloud	ND	ND	ND	MC	MC	MC	MC	ND	ND
G1.683-0.089	1.6° cloud	–	ND	ND	MC	MC	MC	–	MC	MC
G359.137+0.031	isolated HMSF candidate	C	–	C	C	MC	MC	MC	N, GC	MVC, C
G359.484-0.132	Sgr C	IA	–	–	–	–	MC	MC	–	–
G359.611+0.018	far-side stream candidate	–	ND	ND	ND	ND	MC	MC	ND	ND
G359.615-0.243	isolated HMSF candidate	IA	–	C	C	C	C MC	MC	MC	MVC, C
G359.734+0.002	far-side stream candidate	IA	–	C	C	C	MC, C	MC, C	MC	C
G359.865+0.022	far-side stream candidate	–	–	–	–	–	–	–	–	–
G359.889-0.093	20 km s^{-1} Cloud	IA	–	MC	ND	ND	ND	MC	ND	ND
G359.948-0.052	Circumnuclear Disk	–	–	–	–	MC	MC	MC	–	–

Figure 2. Normalized integrated intensity ratios in each region normalized by the integrated intensity of the $C^{18}O$ emission in that region. Representative uncertainties of ± 1 dex are shown, as these integrated intensity ratios likely suffer from both observational and physical uncertainties due to spatial filtering, optical depth effects, etc. OCS (218.9 GHz) has been removed from both this figure and Fig. 3 as it only has a single data point.

the Galactic Centre on $\gtrsim$ pc scales show that bright emission from dense gas tracers (e.g. NH_3, N_2H^+, HCO^+) is extended across the entire CMZ (e.g. Jones et al. 2012; Longmore et al. 2013). However, emission from these dense gas tracers on similar scales in local clouds, such as Orion, is confined to the highest density regions of the clouds (see Lada, Lombardi & Alves 2010; Pety et al. 2017; Kauffmann et al. 2017a; Hacar et al. 2018). The apparent similarity in these observed tracers (H_2CO, OCS, SiO, SO) may therefore indicate a difference in the chemistry between the various tracers, or it may simply be a product of observational uncertainties.

We note, however, several caveats in interpreting this at face value. First, we do not observe the same lines that show these cloud-scale differences in *CMZoom* and therefore cannot rule out that

these differences would present themselves at the core-scale if these lines were observed. Secondly, it is not clear if the high-mass star formation regions observed in the *CMZoom* survey are representative of other such regions throughout the Galaxy. Thirdly, the variation in CMZ integrated intensity ratios may simply be so large that it encompasses the range in typical Galactic disc integrated intensity ratios.

6 LINE PROPERTIES OF 230 GHZ CONTINUUM SOURCES

We now investigate the detection statistics and line properties of the CMZoom 230 GHz continuum sources using the fits to the spectra
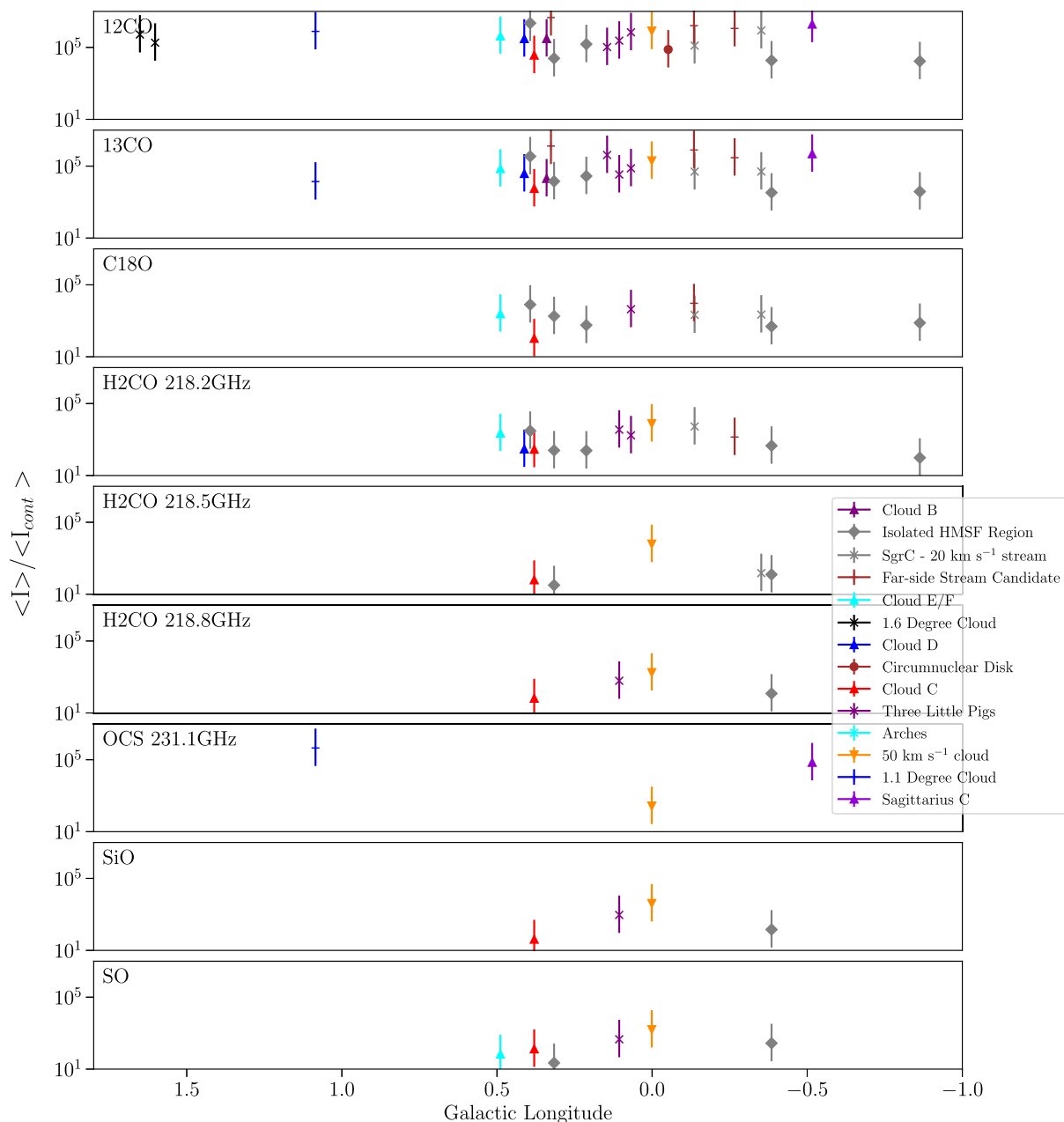
Figure 3. Normalized integrated intensity ratios in each region compared to the 230 GHz continuum. Representative uncertainties of ± 1 dex are shown, as these integrated intensity ratios likely suffer from both observational and physical uncertainties due to spatial filtering, optical depth effects, etc.

for each of the main individual transitions targeted in the CMZoom survey (see Table 1).

6.1 Detection statistics of brightest lines and identification of primary kinematic tracer

Table 1 also shows the detection statistics for each of the key tracers. We note here that the complete number of sources in our data set differs substantially from the complete robust catalogue presented in Paper II, as we have left several larger mosaics – including Sagittarius B2 – out of this analysis until additional steps can be made to suitably clean these. Of the remaining clouds, ^{12}CO and ^{13}CO are detected in 96 per cent of all sources. However, all ^{12}CO and most ^{13}CO data

suffer from image artefacts so they can not be used as reliable tracers for the kinematics of the sources. We remove these transitions in the kinematic analysis from here on.

After ^{12}CO and ^{13}CO, C^{18}O and the lowest energy H$_2$CO transition are the next most often detected, being found in 58 and 82 per cent of all sources, respectively. As these transitions tend to be well correlated, sources with only one of these transitions are interesting targets for potential follow-up observations. As summarized in Table 1, the images of these transitions do not suffer from imaging artefacts and the line profiles are generally well fit with single or multiple Gaussian components. The emission from both of these transitions should therefore provide robust information about the compact source kinematics. Given the prevalence of the lower
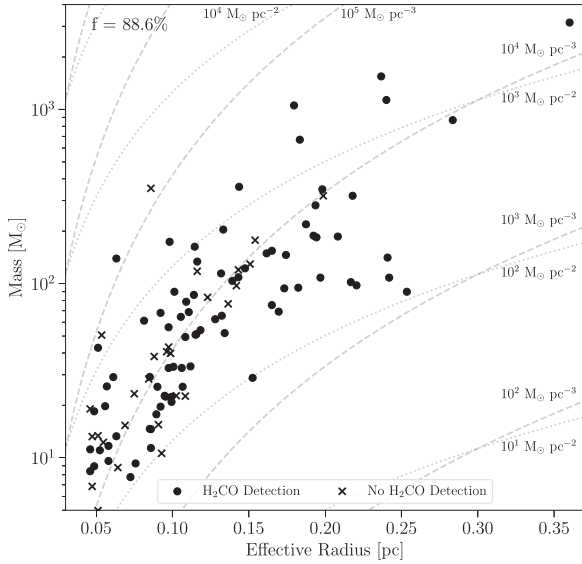
Figure 4. Mass versus effective radius relation with markers indicating sources with a H_2CO (218.2 GHz) detection. The number in the top-left corner states that sources with H_2CO (218.2 GHz) detections account for 88.8 per cent of the mass of all sources in this work. The dashed lines are lines of constant volume density where $10^4 \, M_\odot \, pc^{-3} \sim 1.5 \times 10^5 \, cm^{-3}$, assuming a mean particle mass of 2.8 a.m.u. The detections lie in the range 10^4–$10^6 \, cm^{-3}$. Dotted lines indicate lines of constant column density.

transition of H_2CO and the fewer deviations in line profiles from that well described by a single Gaussian component, we opt to use H_2CO as our fiducial tracer of the compact source kinematics.

Fig. 4 shows the mass–radius relation for all sources included in this analysis, with circles indicating sources with a H_2CO (218.2 GHz) detection. As expected, the larger and more massive sources are more likely to be detected in H_2CO, though this transition is still detected in a majority of small, low-mass sources. Overall, these sources represent 88.8 per cent of the total mass of sources that have been included in this analysis. As such, using this transition as our fiducial tracer provides significant coverage across the whole survey.
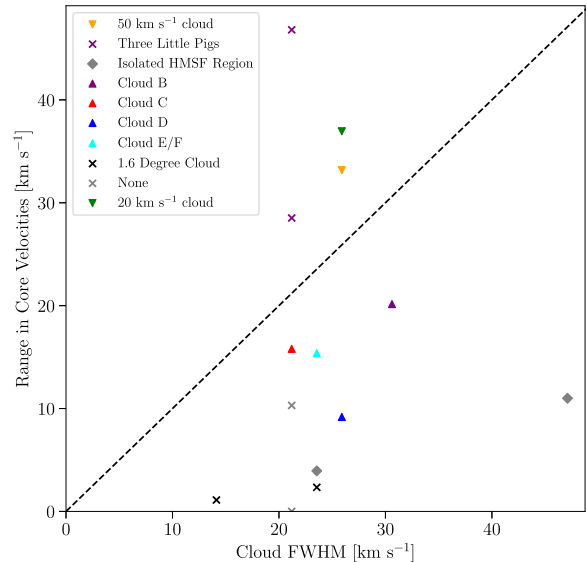
6.2 Analysis of compact source velocities

Fig. 5 shows a histogram of the V_{LSR} difference for each compact source between H_2CO, and all other lines detected detected towards that compact source. The black-dashed line shows the best-fit Gaussian to all data within a V_{LSR} difference $\Delta V_{LSR} \leq 5 \, km \, s^{-1}$. The small mean and dispersion of -0.29 and $1.98 \, km \, s^{-1}$, respectively, gives confidence that the observed V_{LSR} for sources is robust. There are 30 sources with $\Delta V_{LSR} > 5 \, km \, s^{-1}$ which lie in nine clouds throughout the survey. Of these 30 sources, 12 of them belong to G359.889–0.093, five to G0.001–0.058, and four to G0.068–0.075 – i.e. they lie very close in projection to the Galactic Centre. This is the most complicated part of position–position-velocity space, with multiple, physically distinct components along the line of sight, so these V_{LSR} offsets are not unexpected (Henshaw et al. 2016b).

We then seek to understand how these compact source V_{LSR} values compare to the observed velocities of their parent clouds on larger scales. In order to determine a representative velocity range for each parent cloud, we use the catalogue of Walker et al. (in prep.) who extracted spatially averaged spectra for each cloud from single-dish
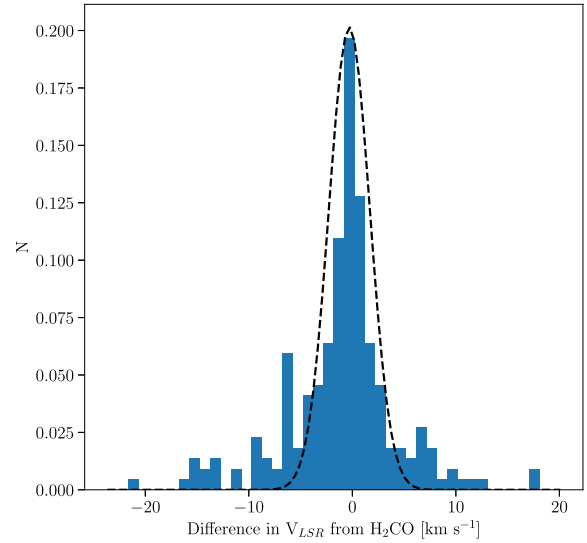
Figure 5. Histogram of the V_{LSR} difference of each key transition when compared to the lower transition of H_2CO for every compact source. The dashed line represents a Gaussian fit to the mean and standard deviation – $(\mu, \sigma = -0.29, 1.98)$ – of the data.

Figure 6. Comparison of the range in compact source velocities of the 10 key transitions targeted by the survey as measured by SCOUSEPY to the observed FWHM of the cloud. The dashed line shows the one-to-one line. The majority of sources fall below the dashed line, as expected if these sources are distributed within the cloud. In the main text, we discuss each of the clouds which lie above the dashed line.

data in the literature. To do this, they used archival data from the APEX CMZ survey at 1 mm (Ginsburg et al. 2016), and the MOPRA CMZ survey at 3 mm (Jones et al. 2012). The results used here are specifically from the Gaussian fits to the integrated spectra of the HNCO $(4_{0,4}–3_{0,3})$ emission.

Fig. 6 compares the full-width half maximum (FWHM) of the Walker et al. (in prep.) single-dish observations to the range of observed compact source velocities within the same cloud, using only the compact source velocities measured for the 10 key transitions

described in Table 1. The dashed line shows the one-to-one relation between those velocities. In general, we would expect the range of compact source velocities within a cloud to be similar to or smaller than the cloud's FWHM if the sources lie within the parent cloud, i.e. points should lie below the one-to-one line. As expected, most of the clouds satisfy this criteria.

Two of the four clouds that do not meet this criteria are the 20 and 50 km s^{-1} clouds. This is somewhat expected, first as these clouds are composed of large mosaics (67 and 24 pointings, respectively). Secondly, these clouds have large velocity gradients across them, causing the compact source velocities on one side of the region to differ significantly from the other side. Such velocity gradients are expected due to the evolution of gas clouds under the influence of the external gravitational potential (see e.g. Kruijssen, Dale & Longmore 2015; Dale, Kruijssen & Longmore 2019; Kruijssen et al. 2019; Petkova et al. 2021).

The 'Three Little Pigs' clouds that lie above the one-to-one line, however, are small and do not have large velocity gradients across them. The region farthest above the one-to-one line – 'G0.068-0.075' – contains 12 dense sources identified by Paper II. To try and understand the much larger than expected range in compact source velocities, we inspect the individual spectra for this region in detail.

Fig. E4 shows the spectra extracted from each spectral cube of the most massive compact source (G0.068–0.075a) in which ^{13}CO, C^{18}O, H$_2$CO (218.2 GHz), and SiO all peak at $\sim$20 km s^{-1} differing from the average V_{LSR} of the remaining sources within the cloud by $\sim$30 km s^{-1}. Fig. E5 shows the same spectra for the second most massive compact source in the cloud, in which these key transitions peak well within the shaded region indicating the cloud's velocity dispersion. Since this is the case for all sources other than 'a', it suggests that this compact source may not be contained within the cloud, and instead may be unassociated with the cloud identified in Walker et al (in prep.). Henshaw et al. (2016b) identified a second velocity component along the same line of sight as this cloud, separated by $\sim$20 km s^{-1}, which could potentially be the source of these additional features. However, further work is required to understand the nature and location of compact source 'a'.

The fourth cloud above the dashed line, 'G0.106–0.082', contains multiple, broad velocity components in the spectra (Fig. D4). The peak of the CMZoom emission sits within the shaded region showing the cloud's velocity dispersion. However, additional velocity components in most of the transitions lie outside this range. It seems likely that the Walker et al. (in prep.) catalogue only derived the cloud velocity and velocity dispersion from one of these two velocity components.

6.3 Compact source velocity dispersions

Fig. 7 shows a histogram of the velocity dispersion difference for each compact source between H$_2$CO and all other lines detected towards that compact source. The black-dashed line shows the best-fit Gaussian to all data within $\Delta\sigma \leq 4$ km s^{-1}. The small mean and dispersion of 0.15 and 1.41 km s^{-1}, respectively, gives confidence that the observed velocity dispersion for the sources are robust. There are 10 sources with $\Delta\sigma > 4$ km s^{-1} from four different clouds. Of these 10 sources, three belong to G0.001–0.058, three to G0.068–0.075, two to G0.106–0.082, and two to G359.889–0.093. We note that most sources with $\Delta\sigma > 4$ km s^{-1} also have $\Delta V_{LSR} > 5$ km s^{-1}, likely a result of either multiple velocity components being averaged together or poorer fit results from lower signal-to-noise spectra.
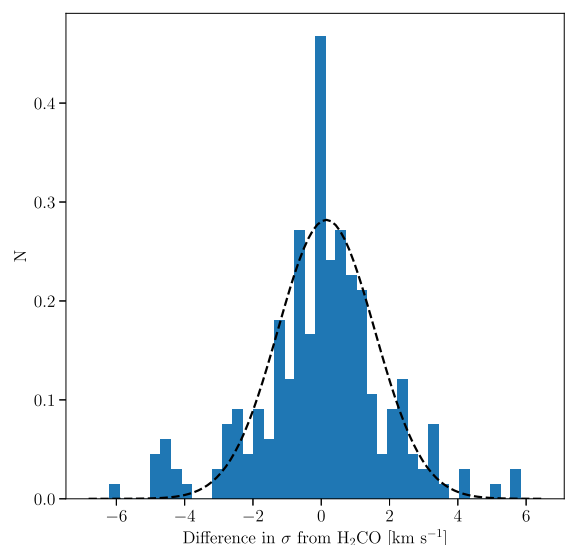

Figure 7. Histogram of the velocity dispersion difference of each key transition when compared to the lower transition of H$_2$CO for every compact source. The dashed line represents a Gaussian fit to the mean and standard deviation – ($\mu, \sigma = 0.15, 1.41$) – of the data.
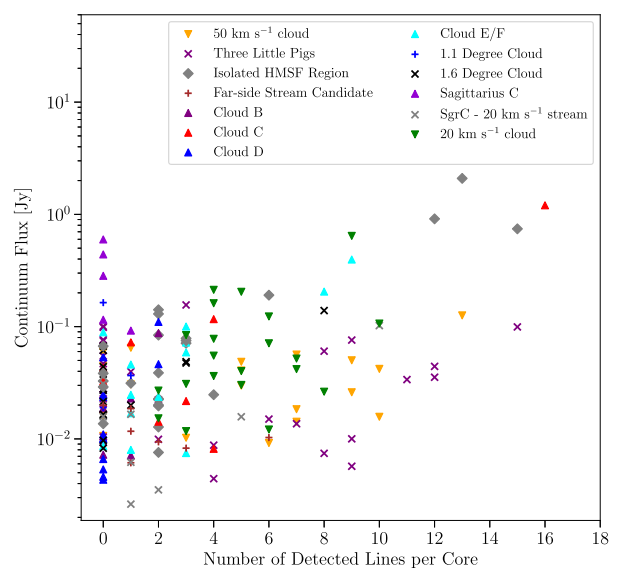
Figure 8. Comparison of the total continuum flux of each dense compact source to the number of total detected lines within the compact source. A general upwards trend implying that the brighter sources tend to have more line complexity.

6.4 Number of lines detected per compact source

Fig. 8 shows the relation between the observed continuum flux of each compact source and the number of spectral lines detected. There is a slightly upward trend showing that the brighter sources tend to have more lines detected. Three of the six observed dense sources within cloud 'b' have no detected emission lines despite having continuum fluxes of $\gtrsim$0.2 Jy. All other sources with such high continuum fluxes have $\geq$9 detected lines. These 'line-deficient, continuum-bright' sources are interesting to follow-up as potential precursors to totally metal stars that have been predicted to exist (Hopkins 2014). A source with bright continuum flux and no line emission suggests that either the gas to dust ratio is very low or
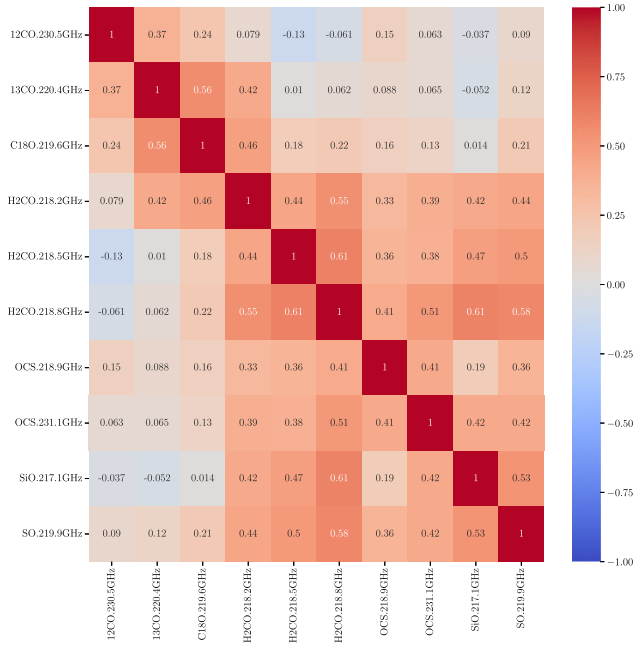
Figure 9. Correlation matrix showing the correlation coefficients between the amplitude of Gaussian peaks fit by SCOUSEPY for the 10 key transitions targeted by the survey.

the line abundances are very low. Very low gas to dust ratios are predicted by the 'totally metal' star scenario, while the latter may highlight sources with interesting chemical or excitation regimes.

Conversely, sources in the 'Three Little Pigs' clouds, and to a lesser extent the 50 km s^{-1} cloud, stand out as having a large number of lines detected at low continuum flux levels. We note that in the right-hand panel of Fig. 12, the sources in both of these clouds lie in the same portion of external pressure versus gas surface density space, and have a similar (low) fraction of star forming sources, with only one or two ambigious tracers of star formation activity. We speculate that the large number of lines detected in sources at low continuum flux levels in the 'Three Little Pigs' clouds and 50 km s^{-1} cloud may be the result of shocks in the high-pressure gas beginning to compress the gas and instigate star formation. Further work is needed to test this hypothesis.

6.5 Correlations between the emission from different transitions

We now investigate how well the emission from the 10 key different transitions correlate with each other. Fig. 9 shows the correlation matrix for the measured amplitudes of the detected emission from these lines. The larger the correlation coefficient shown in each grid cell, the stronger the correlation between the two lines in that row and column. Negative values indicate the emission in the lines is anticorrelated. The correlation coefficient of 1.0 along the diagonal of the matrix shows the autocorrelation of the emission from each line with itself.

We begin by looking at the correlations between the three main 'groups' of transitions – the CO isotopologues, the H_2CO transitions tracing dense gas, and the shock tracers – before investigating the correlations between transitions in different groups.

Unsurprisingly, emission from the three CO isotopologues are well correlated. The imaging artefacts in the ^{12}CO and ^{13}CO data cubes may well contribute to a lower correlation coefficient between these

transitions than may have been expected. Again unsurprisingly, the three H_2CO transitions are also positively correlated, with the highest two energy levels having the highest correlation coefficient of all line pairs. Emission from the SiO, SO, and OCS transitions are all well correlated too. As these transitions trace emission from shocks, these correlation makes sense.

We then turn to comparing correlations between transitions in different groups. The emission from ^{12}CO and ^{13}CO is almost completely uncorrelated (and sometimes even slightly anticorrelated) with the emission from all the other transitions. The only stark exception to this is that emission from ^{13}CO is well correlated with emission from the lowest energy level of H_2CO.

The $C^{18}O$ emission only shows a very weak correlation with most of the other non-CO transitions. Again the notable exception to this is that the $C^{18}O$ emission is well correlated with the lower energy transition of H_2CO. The increasing correlation between the CO isotopologues with the lower energy transition of H_2CO, from ^{12}CO to ^{13}CO to $C^{18}O$, suggests that these transitions are increasingly better tracers of denser gas, as expected given their relative abundances.

Comparing the H_2CO transitions with the shock tracers, there is an apparent increase in correlation with increasing H_2CO transition energy for all shock tracers. This suggests there is a relation between clouds containing dense gas with higher excitation conditions and the prevalence and strength of shocks (Turner & Lubowich 1991; Lu et al. 2021). Such clouds might be expected where there are the convergent points of large-scale, supersonic, colliding gas flows or increased star formation activity. It is interesting that while the 218.5 and 218.8 GHz transitions of H_2CO have nearly identical upper state energies, the 218.8 GHz transition correlates much better with SiO than the other. This apparent trend could be the result of large correlation uncertainties, and these correlations are in fact statistically equivalent. If this is not the case, then it is highlighting a potential problem in interpreting the difference between these lines, as the two upper transitions of H_2CO have the same upper state energy levels and excitation properties, and should therefore be correlated to other transitions by the same amount.

Summarizing the results of the correlation matrix analysis, we conclude that: (i) ^{12}CO (and to a lesser extent ^{13}CO) is a poor tracer of the dense gas; (ii) the $C^{18}O$ and lowest energy H_2CO transition are the most robust tracers of the dense gas; (iii) the higher energy H_2CO transitions and the shock tracers are all consistently pinpointing regions with elevated shocks and/or star formation activity.

7 ANALYSIS

In this section, we use the results of the line fitting and conclusions in Section 6 to determine the likely virial state of the continuum sources (subSection 7.1) and its relation to their star forming potential (subSection 7.2), then search for signs of proto-stellar outflows (subSection 7.3) and intermediate-mass black holes (subSection 7.4) in the CMZoom line data.

7.1 Determining the virial state of the compact continuum sources

As described above, H_2CO (218.2 GHz) was used to determine the kinematic properties for the sources within Paper II's dendrogram catalogue due to its prevalence throughout the survey, and typically being a bright line with a Gaussian profile and a single velocity component. Using the line fit parameters for this transition, we calculated the virial parameter, α, for every source with a H_2CO (218.2 GHz) detection using the observed velocity dispersion (σ_{obs}),
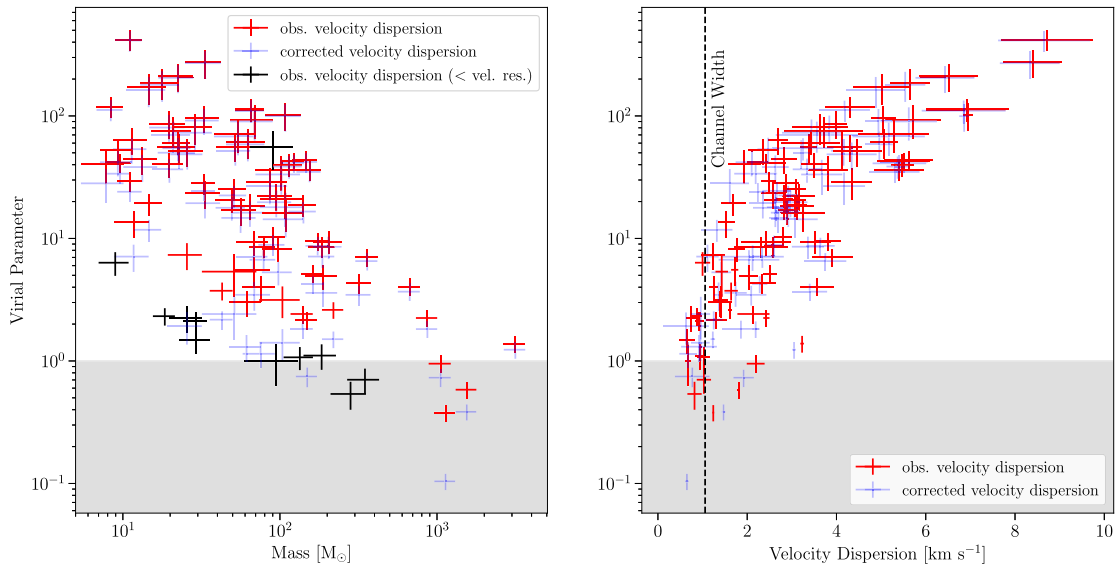
Figure 10. Virial parameters as a function of dendrogram compact source mass [left] and observed velocity dispersion [right]. The red crosses show the observed velocity dispersion, the blue crosses show the velocity dispersion corrected for the instrumental velocity resolution. The black crosses in the left-hand panel show those measurements for which the fit result for the velocity dispersion is lower than the channel width, and thus cannot be corrected for the instrumental velocity resolution. The vertical dashed line in the right-hand panel indicates the channel width of the ASIC data. The shaded grey region represents the condition a compact source must meet to be virially bound. These plots show that when only considering the support from gas kinetic energy against self-gravity, most of the sources are not gravitationally bound. The fact that the measured line widths for most sources are larger than the channel width demonstrates that this result is not affected by the velocity resolution of the observations.

by considering a compact source's kinetic energy support against its own self gravity through,

$$\alpha = \frac{5\sigma^2 R}{GM},$$

(McKee & Tan 2003), where σ is the velocity dispersion, R and M, are the radius and mass of the dendrogram compact source derived in Paper II, and G is the gravitational constant. The constant '5' comes from the simplistic assumption that these sources are uniform spheres, which may not be the case for all sources in the survey.

Fig. 10 shows the distribution of virial parameters as a function of compact source mass and compact source velocity dispersion. Using this form of the virial analysis, only six (out of 103) of the more high-mass sources are virially bound based on observed velocity dispersions, and four are virially bound based on the corrected velocity dispersion. 94–96 per cent of sources in the survey are gravitationally unbound when only considering a compact source's kinetic energy support against its own self gravity. Similar results have been observed in the past by various dynamical studies, with Singh et al. (2021, and references therein) finding there are a number of systematic errors that can affect virial ratio measurements.

To explore if this is a physical representation of the compact source population within the CMZ or a result of the limited velocity resolution of the survey, we first repeated the analysis in Fig. 10 after correcting for the instrumental velocity resolution (blue crosses in Fig. 10). We calculated the virial parameter using the corrected velocity dispersion ($\sigma_{\rm int}$) by subtracting the channel width ($\sigma_{\rm inst}$) in quadrature from the observed velocity dispersion, $\sigma_{\rm int} = \sqrt{\sigma_{\rm obs}^2 - \sigma_{\rm inst}^2}$. The velocity dispersion of most sources are significantly larger than the channel width, so the virial ratios >1 for the majority ($\sim$78 per cent) of sources are not affected by the instrumental velocity resolution.

We then determined what velocity dispersion each compact source would need to have for it to be gravitationally bound, i.e. to have α
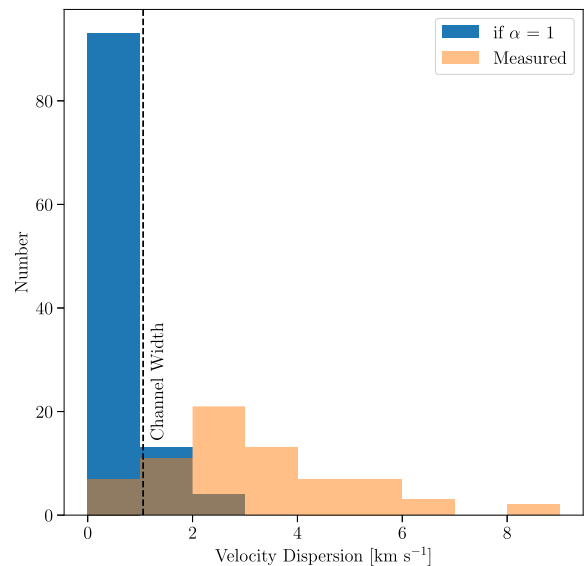
Figure 11. Histogram of measured velocity dispersions (orange) compared to the velocity dispersion required for every compact source to be virially bound (blue). The fact that the observed velocity dispersion is larger than the channel width for most of the sources suggests that the CMZoom velocity resolution is not biasing the virial analysis for most sources. A velocity resolution of $\sim$0.1 km s^{-1} would be required to determine if the small number of sources with linewidths comparable to the CMZ velocity resolution are gravitationally bound.

= 1. Fig. 11 shows a histogram of these '$\alpha = 1$' velocity dispersions compared to the measured velocity dispersions of the sources. This shows that in order to unambiguously determine the virial state of those sources with σ close to the channel width of 1.1 km s^{-1} requires re-observing them with an instrumental velocity resolution
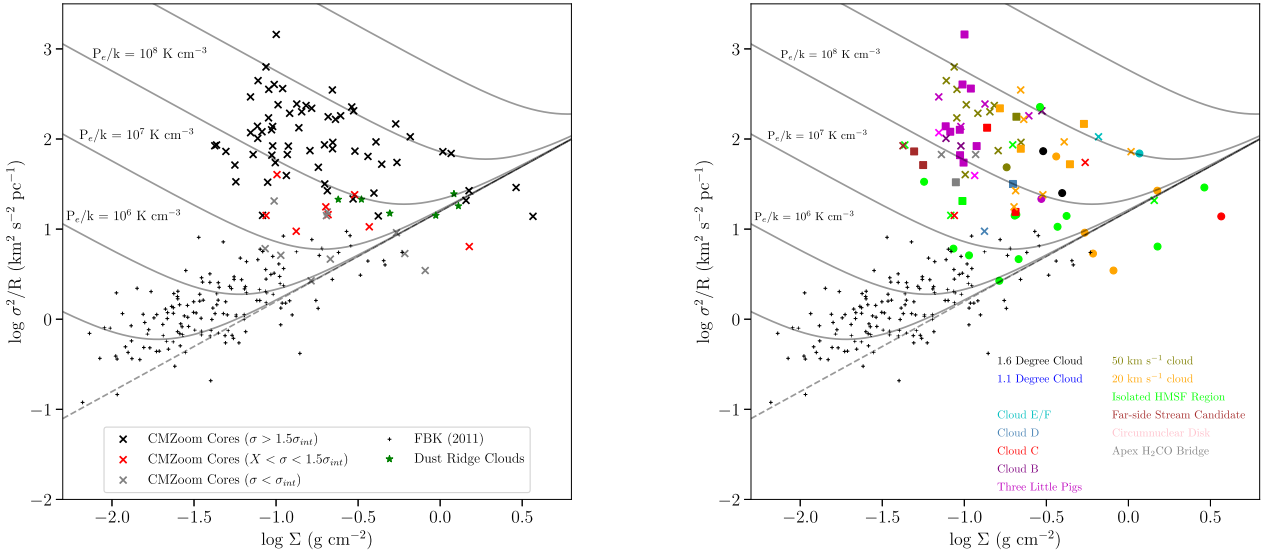
Figure 12. Left: Comparison of the CMZoom sources shown by crosses to Galactic Ring Survey clouds (Field, Blackman & Keto [2011]) shown by black plus symbols. Grey crosses indicate sources with a velocity dispersion less than the channel width ($\sigma_{int} = 1.2\,km\,s^{-1}$) of the survey. Red crosses indicate sources with only slightly resolved velocity dispersions between 1 and 1.5 times the channel width. The black crosses indicate lines with a velocity disperion more than 1.5 times the channel width, so are well resolved. Overlaid are green star markers corresponding to Walker et al. ([2018])'s measurements of dust ridge clouds. The dashed line represents virial equilibrium with $P_e = 0$, and the curved lines represent objects in hydrostatic equilibrium at the stated pressure. While few of the CMZoom sources would be self-gravitating with $P_e = 0$, at pressures of $P_e = 10^8\,K\,km^{-1}$, the majoriry of these sources would be in hydrostatic equilibrium. Right: Left-hand panel with marker colours indicating different key clouds throughout the CMZ. Circles indicate sources that have associated star formation tracers according to Hatchfield et. al. (in prep) or Lu et al. ([2015]), squares indicate sources with potential star formation tracer association according to Hatchfield et. al. (in prep) and crosses indicate sources with no star formation tracer association. All sources, except for one isolated HMSF core, below or close to $P_e = 0$ (shown by the dashed line) are found to be star forming, while the fraction of sources that are star forming drops off quickly against increased pressure or distance above this line.

of $\sim$0.1 km s^{-1} to resolve the smallest plausible sound speed of $\sim$0.2 km s^{-1}. We highlight these low velocity dispersion sources as particularly interesting to follow-up in the search for potential sites of star formation activity with the CMZ.

Having concluded these high virial ratios are real for the majority of sources, we then seek to understand whether these sources are simply transient overdensities, or longer-lived structures. Previous work on the clouds within the dust ridge by Walker et al. ([2018]) and Barnes et al. ([2019]) found that while dust ridge clouds are gravitationally unbound according to virial metrics comparing the gravitational potential and kinetic energies, the intense pressure inferred within the CMZ is sufficient to keep these sources in hydrostatic equilibrium.

In Fig. [12], we replicate the fig. 4 of walker et al. ([2018]) – which in turn replicated fig. 3 of Field et al. ([2011]) – for all sources in the CMZoom survey with a detected $H_2CO(218.2\,GHz)$ transition. The black curved lines show where sources would be in hydrostatic equilibrium if confined by external pressures described by,

$$V_0^2 = \frac{\sigma^2}{R} = \frac{1}{3}\left(\pi\Gamma G\Sigma + \frac{4P_e}{\Sigma}\right), \tag{1}$$

where V_0 is the linewidth-size scaling relation, σ and R are the velocity dispersion and radius of the compact source, Γ is a form factor related to the density structure (as described by Elmegreen [1989]) and here we adopt $\Gamma = 0.73$, which describes an isothermal sphere at critical mass, Σ is the mass surface density, G is the gravitational constant, and P_e is the external pressure. The black-dashed line represents the simple virial condition of $P_e = 0$ as shown in Fig. [10].

Given the gas pressure in the CMZ of $10^{7-9}\,K\,cm^{-3}$, calculated by (Kruijssen et al. [2014]) based on observations by Bally et al. ([1988]), Fig. [12] further enforces the conclusion of Walker et al. ([2018]) that while only a small number of these sources are gravitationally bound according to simply virial analysis, the intense pressures found within the CMZ are capable of keeping a large fraction of these sources in hydrostatic equilibrium, so they may still be long-lived structures.

7.2 The relation of compact source gas kinematics to a compact source's star forming properties

We then seek to understand what role, if any, the kinematic state of the gas plays in setting the star formation potential of the sources. The right-hand panel of Fig. [12] repeats the left, but with marker colours representing a number of key structures throughout the CMZ. Hatchfield et. al. (in prep) use a number of standard high-mass star formation tracer catalogues including methanol masers (Caswell et al. [2010]), water masers (Walsh et al. [2014]), 24 µm point sources (Gutermuth & Heyer [2015]) and 70 µm point source (Molinari et al. [2016]) catalogues to identify which dense sources within Paper II's catalogue may be associated with ongoing star formation. They defined three categories: sources definitely associated with these high-mass star formation tracers, sources definitely not associated with these star formation tracers, and an 'ambiguously star-forming' category for sources where it was difficult to determine whether the observed star formation tracer was associated with that compact source or not. We combined these star formation tracer activities with targeted observations of the 20 km s^{-1} cloud from Lu et al. ([2015]), who detected a number of deeply embedded H_2O masers towards this cloud. In the right-hand panel of Fig. [12], sources with
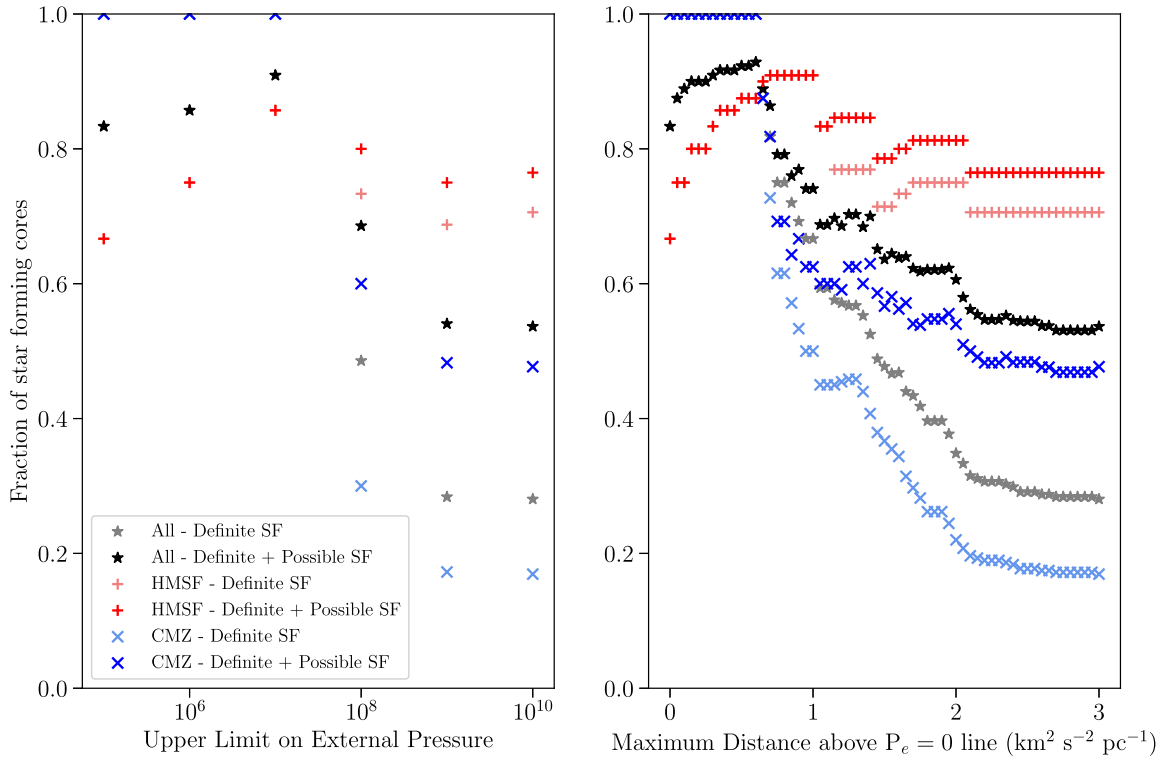
Figure 13. Fraction of sources that are star forming as a function of upper limit on the external pressure [left] or maximum distance above the $P_e = 0$ line [right]. Grey markers indicate all sources with definitive star formation tracers, while black markers indicate all sources with definitive or possible star formation tracers. In addition to this, light red markers indicate isolated HMSF sources with definitive star formation tracers, and dark red markers indicates isolated HMSF sources with definitive or potential star formation tracers. Finally, light blue markers indicate CMZ sources that have definite star formation tracers and dark blue indicates sources with definite or possible star formation tracers.

robust associated star formation tracers are marked with a filled circle. Ambiguously star-forming sources are marked with a square. Sources with a robust non-detection of any star formation tracers are marked with crosses.

We find that all CMZ sources below the $P_e = 0$ line, i.e. all sources with $\alpha \leq 1$, are associated with a star formation tracer. As sources move upwards and to the left of the $P_e = 0$ line, the fraction of sources with star formation tracers drops to ~40 per cent.

We then try to quantify if there is a combination of physical properties that can be used to determine the likelihood that a given compact source will be star forming or not. Fig. 13 shows the fraction of sources that are star forming below lines of constant pressure (left) or as a function of distance from the $P_e = 0$ line (right). We show the total population of sources in black stars, as well as breaking down the population of sources into CMZ sources (blue crosses) and isolated HMSF sources (red pluses). In addition to this breakdown, we have also split these fractions up into regions that show definite association with star formation tracers, indicated by light coloured markers, as well as sources with either definite or ambiguous star formation tracers in dark coloured markers.

All CMZ sources below a maximum external pressure of 10^7 K cm^{-3} have associated star formation tracer activity while the isolated HMSF sources peak at 10^7 K cm^{-3} before plateauing at 70–80 per cent while the CMZ sources drop to 20–50 per cent. These isolated HMSF regions were selected due to their potential star formation activity, so it is no surprise that this population of sources differ significantly from CMZ sources. A similar trend occurs as a function of star forming sources against maximum distance from $P_e = 0$, though the CMZoom sources separate from the isolated HMSF

regions at a faster rate than as a function of external pressure. This suggests that while the external pressure factors in to whether or not a compact source will begin to form stars, the proximity of a compact source to being virially bound provides a more accurate indication of its star formation activity.

7.3 Searching for proto-stellar outflows

The CMZoom spectral set-up was specifically selected to target a number of classic outflow tracers; SiO (Schilke et al. 1997; Gueth, Guilloteau & Bachiller 1998; Codella et al. 2007; Tafalla et al. 2015) and CO (Beuther, Schilke & Stanke 2003). The energies involved in protostellar outflows are sufficiently high enough to vaporize SiO dust grain mantles, and while CO is more prevalent and excited at lower temperatures, it has been used to observe protostellar outflows towards high-mass star forming clouds in the past (e.g. Beuther et al. 2003).

As the most detected transition within the quality controlled data set, and with the most reliable line profiles, we first used H$_2$CO (218.2 GHz) to provide a single V_{LSR} for each compact source. Combining this with the l and b positions from paper II, we generated $\{l, b, V_{LSR}\}$ positions for a large majority of the sources within Paper II's robust catalogue. These data were then overlaid on non-primary beam corrected[5] 3D cubes of SiO and the three CO isotopologues within *glue*.[6] Each compact source was then examined by eye to

---

[5]The increased noise at the edge of the primary beam corrected images obscured the outflow emission.
[6]https://glueviz.org
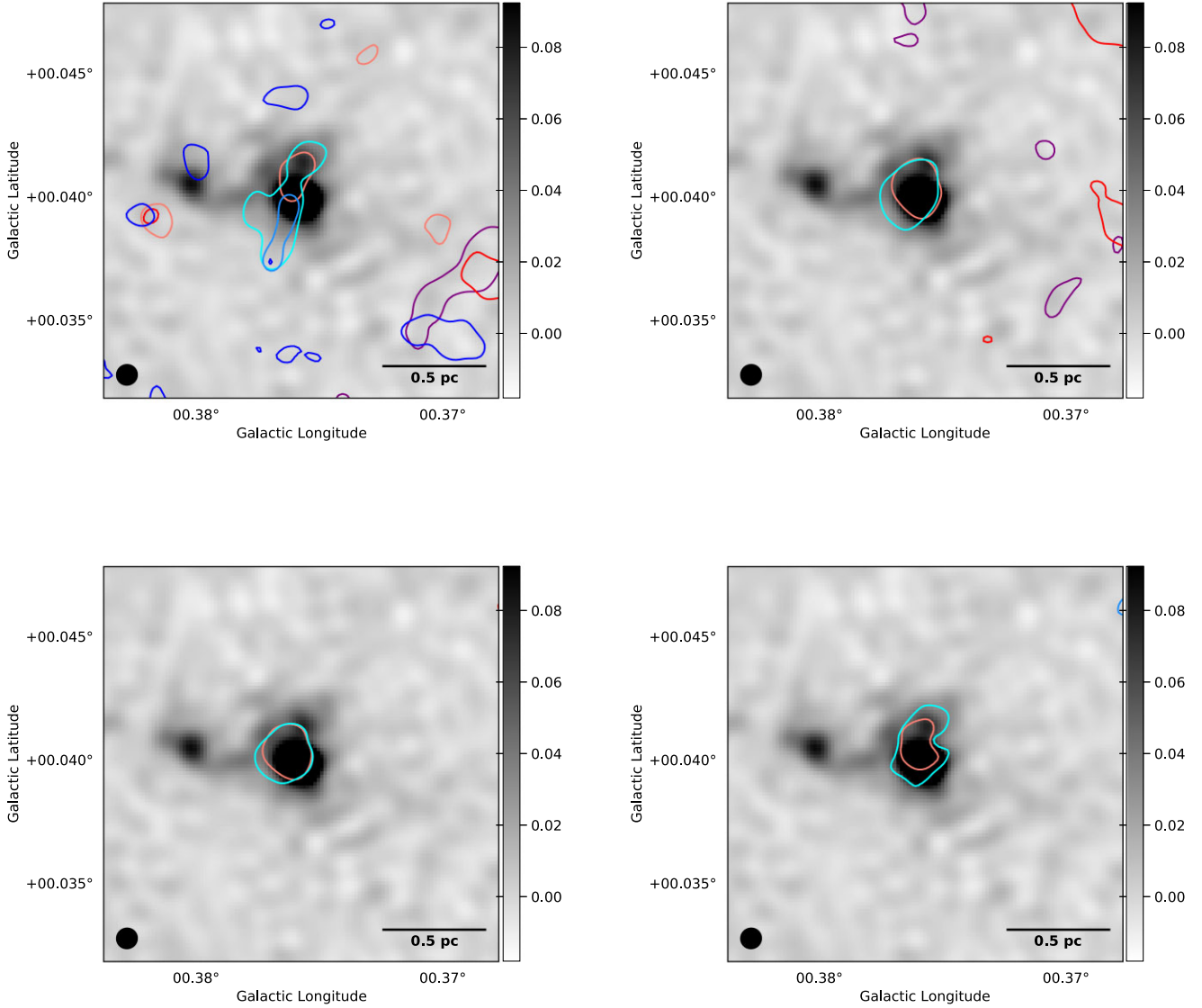
Figure 14. The grey scale images show the 230 GHz continuum emission centred on the most massive compact source within G0.380+0.050. The colour bar shows the flux density in Jy. Overlaid are contours of moment maps produced over 10 km s^{-1} intervals from ± 30 km s^{-1} from the compact source's V_{LSR}, for ^{12}CO (top-left), ^{13}CO (top-right), C^{18}O (bottom-left), and SiO (bottom-right).

check for extended structure along the velocity axis. During this process, only two convincing outflows were detected in clouds G0.380+0.050 and G359.615–0.243 as shown in Figs 14 and 15.

These two clouds were followed up by creating a series of moment maps for SiO and the three CO isotopologues over 10 km s^{-1} intervals across the surrounding ± 30 km s^{-1} from the compact source V_{LSR}. Figs 14 and 15 show these moment maps as contours overlaid on the 230 GHz continuum emission for G0.380+0.050 and G359.615–0.243. While ^{12}CO emission shows evidence of red/blue lobes surrounding the compact source at 30 per cent of peak brightness, there is no sign of similar outflow morphology in any other transition, despite other work having identified an outflow at this compact source in SiO emission. However, Widmann et al. (2016) cautions the use, and in particular the absence, of SiO in interpreting outflows.

The emission in SiO and the three CO isotopologues of 359.615–0.243 all show consistent structures in the form of a significant red lobe to the left of the compact source. The lack of a strong blue

lobe on the opposite side of the compact source may be the result of sensitivity, opacity or different excitation conditions.

We also search for outflow candidates in a more automated way. For every region in the survey, a representative velocity is measured by fitting Gaussian components to a spatially-averaged spectrum of the HNCO emission from the MOPRA CMZ survey (Jones et al. 2012). Using this velocity, we then create blue and red-shifted maps of four different tracers (^{12}CO, ^{13}CO, C^{18}O, and SiO) by integrating the emission over 10 km s^{-1} either side of the V_{lsr} (± 1 km s^{-1}). The blue and red-shifted maps were then combined for each region, and inspected to search for any potential outflow candidates.

Overall, six candidates were identified using this method. Figs F1–F6 show the integrated emission for each of the four molecular line tracers for all 6 candidates, along with ^{12}CO position-velocity plots taken along the candidate outflows. The PV-plots in particular reveal that only 3 of these are likely to be molecular outflows, namely those in G0.316–0.201, G0.380+050, and G359.615–0.243. The latter two of these are the same as those identified via visual inspection in *glue*.
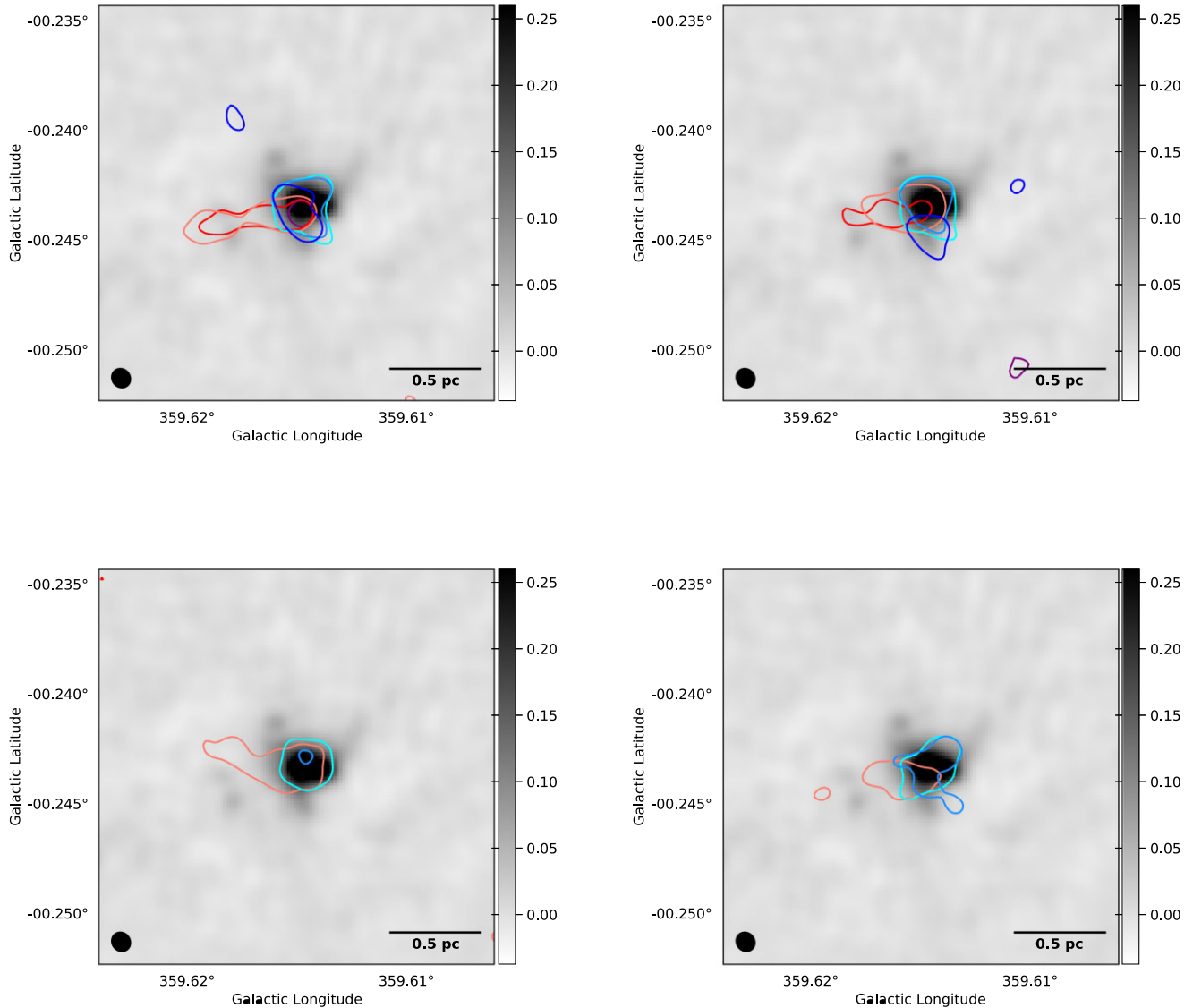
Figure 15. The grey scale images show the 230 GHz continuum emission centred on the most massive compact source within G359.615+0.243. The colour bar shows the flux density in Jy. Overlaid are contours of moment maps produced over 10 km s^{-1} intervals from ± 30 km s^{-1} from the compact source's V_{LSR}, for ^{12}CO (top-left), ^{13}CO (top-right), C^{18}O (bottom-left), and SiO (bottom-right).

Of the three regions with robust outflow detections, only 1 is actually known to be in the CMZ. In Paper I, it was concluded that both G0.316–0.201 and G359.615+0.243 do not reside in the CMZ based on their kinematics and comparison with results from Reid et al. (2019). The only molecular outflow(s) that we detect in the CMZ is therefore in G0.380+0.050 (aka dust ridge cloud C), which is a known high-mass star-forming region (Ginsburg et al. 2015).

Recently ∼50 molecular outflows have been detected across four molecular clouds in the CMZ with ALMA at 0.1–0.2 arcsec resolution (Lu et al. 2021; Walker et al. 2021). All of these clouds are targeted with *CMZoom*, yet we do not detect any of the outflows detected with ALMA. This is likely due due a combination of angular resolution and sensitivity of the SMA data. Indeed, many of the outflows reported are <0.1 pc in projected length, and would not be resolved by our observations. However, some of the larger-scale outflows reported in Lu et al. (2021) are much larger than our resolution, suggesting that they are fainter than our detection limit. Given that the only CMZ-outflow detected with *CMZoom* is in a

high-mass star-forming region, this indicates that our observations are capable of detecting large, bright outflows from massive YSOs only.

In conclusion, *CMZoom* provides the first systematic, sub-pc-scale search for high-mass proto-stellar outflows within the CMZ. We detect only three outflows throughout the survey – one in a known high-mass star forming region, and two more in isolated high-mass star forming regions that are likely not in the CMZ. We can therefore rule out the existence of a wide-spread population of *high-mass* stars in the process of forming that has been missed by previous observations, e.g. due to having low luminosity of weak/no cm-continuum emission.

7.4 Intermediate mass black holes

Intermediate mass black holes (IMBHs) are considered to be the missing link between stellar-mass black holes and supermassive black holes (SMBHs), with multiple merging events of smaller 'seed'
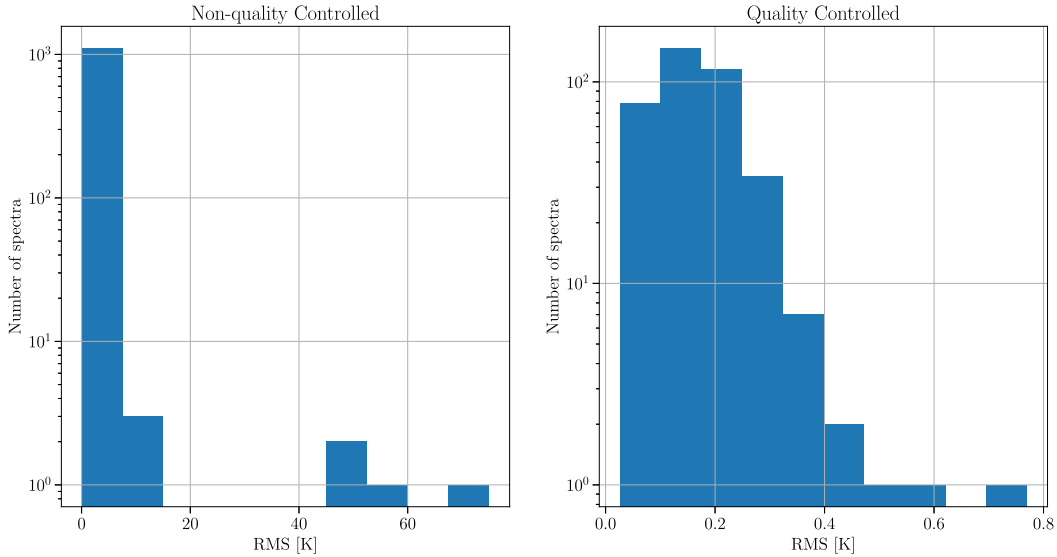
Figure 16. Histogram of the RMS of every spectra throughout the survey measured in Kelvin. The quality controlled data set peaks at ∼0.2 K.

IMBHs growing to form SMBHs (Takekawa et al. 2021). Despite this, their existence has yet to be confirmed. A number of IMBH candidates have been identified in the CMZ via the observation of 'high-velocity compact clouds', or HVCCs. These are dense gas clouds (<5 pc) with high brightness temperatures and large velocity dispersions ($\sigma > 50$ km s^{-1}) (Oka et al. 1998, 2012; Tokuyama et al. 2019), and have been interpreted as the signpost of an intermediate mass black hole (IMBH) passing through a gas cloud and interacting with the gas. As the first sub-pc-scale resolution survey of the dense gas across the whole CMZ, CMZoom is ideally placed to find such HVCCs.

To determine CMZoom's ability to detect such HVCCs, we turn to the papers reporting detections of IMBHs through this method. Oka et al. (2016) reported a compact ($\leq$1.6 pc, using the NRO telescope with a half-power beamwidth of 20 arcsec) candidate IMBH detected in HCN and SiO with an extremely broad velocity width ($\lesssim$100 km s^{-1}), located 0°.2 south-east of Sgr C. Using the volume density of N(H$_2$) $\geq 10^{6.5}$ cm $^{-3}$ given by Oka et al. (2016), we estimate column densities of three of our dense gas tracers – ^{13}CO, C^{18}O and H$_2$CO, assuming standard abundance ratios ([^{13}CO]/[H$_2$] =2 $\times$ 10^{-6}, Pineda, Caselli & Goodman (2008), [C^{18}O]/[H$_2$] = 1.7 $\times$ 10^{-7} Frerking, Langer & Wilson (1982) and [H$_2$CO]/[H$_2$] =10^{-9}, van der Tak, van Dishoeck & Caselli (2000)). Using these column densities, a kinetic temperature of 60 K and a linewidth of 20 km s^{-1}, we use RADEX (van der Tak et al. 2007) to estimate a brightness temperature of between 16–40 K for the interacting gas around this IMBH candidate.

Assuming a typical beam size of 3 × 3 arcsec at a frequency of 230 GHz, we calculate the RMS for each spectra in K, as shown in Fig. 16, which peaks at ∼0.2 K. If the HVCC reported in Oka et al. (2016) is representative of IMBH candidates at these transitions in terms of brightness temperature and size we would expect to easily detect ∼1 pc features using the CMZoom survey. However, even before quality control, we find no spectral components fit with velocity dispersions $\geq$20 km s^{-1} throughout the data. The only exceptions are from protostellar outflows.

In summary, we can rule out the presence of HVCC's or IMBH's with properties like those in Oka et al. (2016) within the region covered by this work.

8 CONCLUSIONS

We present 217–221 and 229–233 GHz spectral line data from the SMA's Large Program observing the Galactic Centre, *CMZoom*, and the associated data release. This data extends the work of previous papers published from this survey – the 230 GHz dust continuum data release and a dense compact source catalogue.

These data were imaged via a pipeline that is an extension to the previously developed imaging pipeline built for the 230 GHz dust continuum data. During this process, a number of clouds – in particular Sagittarius B2 and the Circumnuclear Disk – were found to suffer from severe imaging issues, which prevented these clouds from being analysed. Once imaged, all data were examined by eye to identify both imaging artefacts as well as potentially interesting structures. The quality controlled data were then used to produce moment maps for each cloud, as well as spectra for most dense sources identified by Paper II.

Using SCOUSEPY (Henshaw et al. 2016a, 2019), these spectra were fit and then quality controlled to remove spurious fit results before being used to extract kinematic information for a majority of these dense sources and also identify a number of spectral lines beyond the 10 major transitions of dense gas and shocks that were targeted by *CMZoom*.

By measuring the normalized integrated intensity with respect to both C^{18}O and 230 GHz dust continuum, we find that the shock tracers, SiO and SO, as well as the two higher energy H$_2$CO transitions increase by several orders of magnitude towards the Galactic Centre. We also find that the population of isolated HMSF sources that were included in the survey due to their association with star formation tracers, but which likely lie outside the Galactic Centre, have indistinguishable integrated intensity ratios from the CMZ sources. This may present an interesting avenue for follow-up studies using chemical and radiative transfer modelling to disentangle the opacity and excitation effects, and make a quantitative comparison between the physical conditions within the CMZ and the (foreground) Galactic Disc star-forming regions we have identified. Doing so could have important implications for understanding the similarities and differences in the processes controlling star formation between the two (potentially very different) environments.

We identified H$_2$CO (218.2 GHz) as the best tracer of compact source kinematics, due both to the frequency with which it was detected in sources, but also its tendency to be fit by single Gaussian components. Using this transition, we determine a single V_{LSR} and velocity dispersion for every compact source where H$_2$CO was detected and calculated a virial parameter for each compact source. Using a simple virial analysis, only four dense sources were found to be gravitationally bound.

Expanding this analysis to factor in external pressure and compare this to sources identified as having associated star formation tracers, we find most sources appear to be consistent with being in hydrostatic equilibrium given the high external pressure in the CMZ. All sources below a maximum external pressure of 10^7 K cm^{-3} have associated star formation activity. Above this pressure, the fraction of star forming sources drops. We find that the fraction of star forming sources drops even more steeply the farther it lies from virial equilibrium. We conclude that while the external pressure plays a role in determining whether or not a compact source will begin to form stars, how close a compact source is to being gravitationally bound provides a more accurate indication of its star formation activity.

Through visual inspection of the three CO isotopologues and SiO, only two protostellar outflows (in clouds G0.380+0.050 and G359.614+0.243) were detected throughout the entire survey. We can therefore rule out a wide-spread population of high-mass stars in the process of forming that has been missed by previous observations, e.g. due to having low luminosity of weak/no cm-continuum emission

Recent observations of the CMZ have highlighted a number of high-velocity compact clouds (HVCCs) which have been interpreted as candidate intermediate mass black holes (IMBHs). Despite having the sensitivity and resolution to detect such HVCCs, we do not find any evidence for IMBHs within the *CMZoom* survey spectral line data.

ACKNOWLEDGEMENTS

DATA AVAILABILITY

The data underlying this article will be made available via dataverse, at https://doi.org/10.7910/DVN/SPKG2S.

REFERENCES

Bally J. et al., 2010, ApJ, 721, 137
Bally J., Stark A. A., Wilson R. W., Henkel C., 1988, ApJ, 324, 223
Barnes A. T. et al., 2019, MNRAS, 486, 283
Barnes A. T. et al., 2021, MNRAS, 503, 4601
Barnes A. T., Longmore S. N., Battersby C., Bally J., Kruijssen J. M. D., Henshaw J. D., Walker D. L., 2017, MNRAS, 469, 2263
Battersby C. et al., 2020, ApJS, 249, 35
Beuther H., Schilke P., Stanke T., 2003, A&A, 408, 601
Caswell J. L. et al., 2010, MNRAS, 404, 1029

Codella C., Cabrit S., Gueth F., Cesaroni R., Bacciotti F., Lefloch B., McCaughrean M. J., 2007, A&A, 462, L53
Dale J. E., Kruijssen J. M. D., Longmore S. N., 2019, MNRAS, 486, 3307
Dame T. M., Hartmann D., Thaddeus P., 2001, ApJ, 547, 792
Elmegreen B. G., 1989, ApJ, 338, 178
Field G. B., Blackman E. G., Keto E. R., 2011, MNRAS, 416, 710
Frerking M. A., Langer W. D., Wilson R. W., 1982, ApJ, 262, 590
Ginsburg A. et al., 2015, A&A, 584, L7
Ginsburg A. et al., 2016, A&A, 586, A50
Ginsburg A. et al., 2018, ApJ, 853, 171
Gueth F., Guilloteau S., Bachiller R., 1998, A&A, 333, 287
Gutermuth R. A., Heyer M., 2015, AJ, 149, 64
Hacar A., Tafalla M., Forbrich J., Alves J., Meingast S., Grossschedl J., Teixeira P. S., 2018, A&A, 610, A77
Hatchfield H. P. et al., 2020, ApJS, 251, 14
Henshaw J. D. et al., 2016a, SCOUSE: Semi-automated multi-COmponent Universal Spectral-line fitting Engine (ascl:1601.003)
Henshaw J. D. et al., 2016b, MNRAS, 457, 2675
Henshaw J. D. et al., 2019, MNRAS, 485, 2457
Henshaw J. D., Barnes A. T., Battersby C., Ginsburg A., Sormani M. C., Walker D. L., 2022, preprint (arXiv:2203.11223)
Hopkins P. F., 2014, ApJ, 797, 59
Jackson J. M. et al., 2013, PASA, 30, e057
Jones P. A. et al., 2012, MNRAS, 419, 2961
Kauffmann J., Pillai T., Zhang Q., Menten K. M., Goldsmith P. F., Lu X., Guzmán A. E., 2017a, A&A, 603, A89
Kauffmann J., Pillai T., Zhang Q., Menten K. M., Goldsmith P. F., Lu X., Guzmán A. E., Schmiedeke A., 2017b, A&A, 603, A90
Krieger N. et al., 2017, ApJ, 850, 77
Kruijssen J. M. D. et al., 2019, MNRAS, 484, 5734
Kruijssen J. M. D., Dale J. E., Longmore S. N., 2015, MNRAS, 447, 1059
Kruijssen J. M. D., Longmore S. N., 2013, MNRAS, 435, 2598
Kruijssen J. M. D., Longmore S. N., Elmegreen B. G., Murray N., Bally J., Testi L., Kennicutt R. C., 2014, MNRAS, 440, 3370
Lada C. J., Lombardi M., Alves J. F., 2010, ApJ, 724, 687
Longmore S. N. et al., 2013, MNRAS, 429, 987
Longmore S. N. et al., 2017, MNRAS, 470, 1462
Lu X. et al., 2017, ApJ, 839, 1
Lu X. et al., 2019, ApJ, 872, 171
Lu X. et al., 2021, ApJ, 909, 177
Lu X., Zhang Q., Kauffmann J., Pillai T., Longmore S. N., Kruijssen J. M. D., Battersby C., Gu Q., 2015, ApJ, 814, L18
McKee C. F., Tan J. C., 2003, ApJ, 585, 850
Mills E. A. C., Battersby C., 2017, ApJ, 835, 76
Mills E. A. C., Ginsburg A., Immer K., Barnes J. M., Wiesenfeld L., Faure A., Morris M. R., Requena-Torres M. A., 2018, ApJ, 868, 7
Mills E. A. C., Morris M. R., 2013, ApJ, 772, 105
Molinari S. et al., 2011, ApJ, 735, L33
Molinari S. et al., 2016, A&A, 591, A149
Morris M., Serabyn E., 1996, ARA&A, 34, 645
Oka T., Hasegawa T., Sato F., Tsuboi M., Miyazaki A., 1998, ApJS, 118, 455
Oka T., Mizuno R., Miura K., Takekawa S., 2016, ApJ, 816, L7
Oka T., Nagai M., Kamegai K., Tanaka K., Kuboi N., 2007, PASJ, 59, 15
Oka T., Onodera Y., Nagai M., Tanaka K., Matsumura S., Kamegai K., 2012, ApJS, 201, 14
Petkova M. A. et al., 2021, MNRAS, preprint (arXiv:2104.09558)
Pety J. et al., 2017, A&A, 599, A98
Pineda J. E., Caselli P., Goodman A. A., 2008, ApJ, 679, 481
Pound M. W., Yusef-Zadeh F., 2018, MNRAS, 473, 2899
Primiani R. A. et al., 2016, J. Astron. Instrum., 05, 1641006
Rathborne J. M. et al., 2015, ApJ, 802, 125
Reid M. J. et al., 2019, ApJ, 885, 131
Rodríguez-Fernández N. J., Martín-Pintado J., Fuente A., Wilson T. L., 2004, A&A, 427, 217
Schilke P., Walmsley C. M., Pineau des Forets G., Flower D. R., 1997, A&A, 321, 293
Singh A. et al., 2021, ApJ, 922, 87

4778   *D. Callanan et al.*

Tafalla M., Bachiller R., Lefloch B., Rodríguez-Fernández N., Codella C., López-Sepulcre A., Podio L., 2015, A&A, 573, L2

Takekawa S., Oka T., Iwata Y., Tsujimoto S., 2021, in Tsuboi M., Oka T.eds, ASP Conf. Ser. Vol. 528, New Horizons in Galactic Center Astronomy and Beyond. Astron. Soc. Pac., San Francisco, p. 149

Tokuyama S., Oka T., Takekawa S., Iwata Y., Tsujimoto S., Yamada M., Furusawa M., Nomura M., 2019, PASJ, 71, S19

Turner B. E., Lubowich D. A., 1991, ApJ, 381, 173

van der Tak F. F. S., Black J. H., Schöier F. L., Jansen D. J., van Dishoeck E. F., 2007, A&A, 468, 627

van der Tak F. F. S., van Dishoeck E. F., Caselli P., 2000, A&A, 361, 327

Walker D. L. et al., 2018, MNRAS, 474, 2373

Walker D. L. et al., 2021, MNRAS, 503, 77

Walsh A. J., Purcell C. R., Longmore S. N., Breen S. L., Green J. A., Harvey-Smith L., Jordan C. H., Macpherson C., 2014, MNRAS, 442, 2240

Widmann F., Beuther H., Schilke P., Stanke T., 2016, A&A, 589, A29

SUPPORTING INFORMATION

Supplementary data are available at *MNRAS* online.

suppl_data

Please note: Oxford University Press is not responsible for the content or functionality of any supporting materials supplied by the authors. Any queries (other than missing material) should be directed to the corresponding author for the article.

[1]*Astrophysics Research Institute, Liverpool John Moores University, 146 Brownlow Hill, Liverpool L3 5RF, UK*
[2]*Harvard-Smithsonian Center for Astrophysics, MS-78, 60 Garden St., Cambridge, MA 02138 USA*
[3]*University of Connecticut, Department of Physics, 196 Auditorium Road, Unit 3046, Storrs, CT 06269 USA*
[4]*ALMA Regional Centre Node, Jodrell Bank Centre for Astrophysics, The University of Manchester, Manchester M13 9PL, UK*
[5]*Max-Planck-Institute for Astronomy, Koenigstuhl 17, D-69117 Heidelberg, Germany*
[6]*Max-Planck-Institut für extraterrestrische Physik, Gießenbachstrae 1, D-85748 Garching, Germany*
[7]*Institut für theoretische Astrophysik, Zentrum für Astronomie der Universität Heidelberg, Albert-Ueberle Str. 2, D-69120 Heidelberg, Germany*
[8]*Department of Astronomy, University of Florida, PO Box 112055, USA*
[9]*Haystack Observatory, Massachusetts Institute of Technology, 99 Millstone Road, Westford, MA 01886, USA*
[10]*Astronomisches Rechen-Institut, Zentrum für Astronomie der Universität Heidelberg, Mönchhofstraße 12-14, D-69120 Heidelberg, Germany*
[11]*Shanghai Astronomical Observatory, Chinese Academy of Sciences, 80 Nandan Road, Shanghai 200030, People's Republic of China*
[12]*Department of Physics and Astronomy, University of Kansas, 1251 Wescoe Hall Dr, Lawrence, KS 66045, USA*
[13]*Boston University Astronomy Department, 725 Commonwealth Avenue, Boston, MA 02215, USA*
[14]*CASA, University of Colorado, 389-UCB, Boulder, CO 80309, USA*
[15]*National Radio Astronomy Observatory, 520 Edgemont Road, Charlottesville, VA 22903, USA*
[16]*Leiden Observatory, Leiden University, PO Box 9513, NL-2300 RA Leiden, the Netherlands*
[17]*Kavli Institute for Astronomy and Astrophysics, Peking University, Beijing 100871, China*
[18]*Department of Astronomy, School of Physics, Peking University, Beijing 100871, China*
[19]*Joint Institute for VLBI ERIC, Oude Hoogeveensedijk 4, NL-7991 PD, Dwingeloo, The Netherlands*
[20]*School of Physics & Astronomy, E.C. Stoner Building, The University of Leeds, Leeds LS2 9JT, UK*
[21]*National Radio Astronomy Observatory, 1003 Lopezville Rd., Socorro, NM 87801, USA*

This paper has been typeset from a TEX/LATEX file prepared by the author.